nature neuroscience

Timing of neurogenesis is a determinant of olfactory circuitry

Fumiaki Imamura[1], Albert E Ayoub[2,3], Pasko Rakic[2,3] & Charles A Greer[1,2]

An odorant receptor map in mammals that is constructed by the glomerular coalescence of sensory neuron axons in the olfactory bulb is essential for proper odor information processing. How this map is linked with olfactory cortex is unknown. Using a battery of methods, including various markers of cell division in combination with tracers of neuronal connections and time-lapse live imaging, we found that early- and late-generated mouse mitral cells became differentially distributed in the dorsal and ventral subdivisions of the odorant receptor map. In addition, the late-generated mitral cells extended substantially stronger projections to the olfactory tubercle than did the early-generated cells. Together, these data indicate that the odorant receptor map is developmentally linked to the olfactory cortices in part by the birthdate of mitral cells. Thus, different olfactory cortical regions become involved in processing information from distinct regions of the odorant receptor map.

The olfactory system, similar to other sensory systems, uses the position of cells in a topographic map to organize and analyze sensory information. Odors detected by olfactory sensory neurons are first relayed to the olfactory bulb glomeruli where the olfactory sensory neuron axons form synapses with the dendrites of projection neurons, the mitral and tufted cells. Because each olfactory sensory neuron expresses only 1 of around 1,200 odorant receptors and olfactory sensory neurons that express the same odorant receptor converge into only 2 or 3 glomeruli in each olfactory bulb[1–3], the spatial arrangement of glomeruli on the surface of the olfactory bulb establishes an 'odorant receptor map'[4]. Olfactory sensory neurons that express different odorant receptors can also differ in their expression of combinations of molecules that regulate fasciculation, convergence and targeting of axons[5–9]. Thus, although the afferent innervation of an individual glomerulus is molecularly homogeneous, as a population, glomeruli are highly heterogeneous. Therefore, the odorant receptor map can be divided into several distinct zones or domains on the basis of the molecular phenotypes of olfactory sensory neuron axons[8,10,11]. Finally, glomeruli that are activated by odorants with similar molecular features are positioned close together and define clusters in the map[12–14].

Mice in which the olfactory sensory neurons that project to dorsal glomeruli are ablated retain the ability to detect odors but lack fear responses to predator odors[10]. This suggests that olfactory bulb glomeruli in different regions of the odorant receptor map have distinct roles in odor information processing, and this concept is supported by the preservation of odorant receptor maps between the right and left olfactory bulbs in both mice and rats[15,16]. Despite the functional importance of the odorant receptor map, the rules that are used to decode the map by the olfactory bulb projection neurons and olfactory cortices are unknown. It is unlikely that the odorant receptor map is projected directly onto the olfactory cortex; individual odors are sparsely represented in broad regions of piriform cortex, without evidence of clusters[17,18]. The olfactory systems of *Drosophila*[19] and zebrafish[20] show similar representations. Finding the rules that link the maps of odorant receptors in olfactory bulb and in the olfactory cortex is crucial for understanding the anatomical and physiological basis of odor processing in mammals. Previous studies suggested that olfactory cortices receive axons from subpopulations of mitral cells that are non-uniformly distributed throughout the mitral cell layer (MCL); for example, the olfactory tubercle preferentially receives input from mitral cells in the ventral olfactory bulb[21,22]. However, the relationship between the distribution of mitral cells that send axons to the olfactory tubercle and the odorant receptor map remains unclear.

We found that mitral cells that have different birthdates are differentially distributed in the dorsomedial and ventrolateral regions of the olfactory bulb, which, as defined by olfactory cell adhesion molecule (OCAM) expression, are correlated with the dorsal and ventral zones of the odorant receptor map. This finding is reminiscent of the birthdate-dependent dendritic targeting of glomeruli by projection neurons in *Drosophila*[23] as well as the presence of areal and laminar neurogenetic gradients among cytoarchitectonic areas in the mammalian neocortex, including those of humans and nonhuman primates[24,25]. We also present evidence that the late-generated mitral cells might migrate tangentially toward postero-ventro-lateral regions in the olfactory bulb, guided by an axonal scaffold. Finally, we show that the olfactory tubercle is preferentially innervated by late-generated mitral cells. These data indicate that the birthdates of mitral cells might determine their location in the MCL and indirectly shape the innervation patterns of olfactory cortices.

RESULTS

Mitral cell location and birthdate

To determine mitral cell birthdates we used one of three thymidine analogs (XdU): BrdU, CldU or IdU, which label cells in the S-phase

[1]Department of Neurosurgery, Yale University School of Medicine, New Haven, Connecticut, USA. [2]Department of Neurobiology, Yale University School of Medicine, New Haven, Connecticut, USA. [3]The Kavli Institute of Neuroscience, Yale University School of Medicine, New Haven, Connecticut, USA. Correspondence should be addressed to C.A.G. (charles.greer@yale.edu).

Received 25 October 2010; accepted 11 January 2011; published online 6 February 2011; doi:10.1038/nn.2754

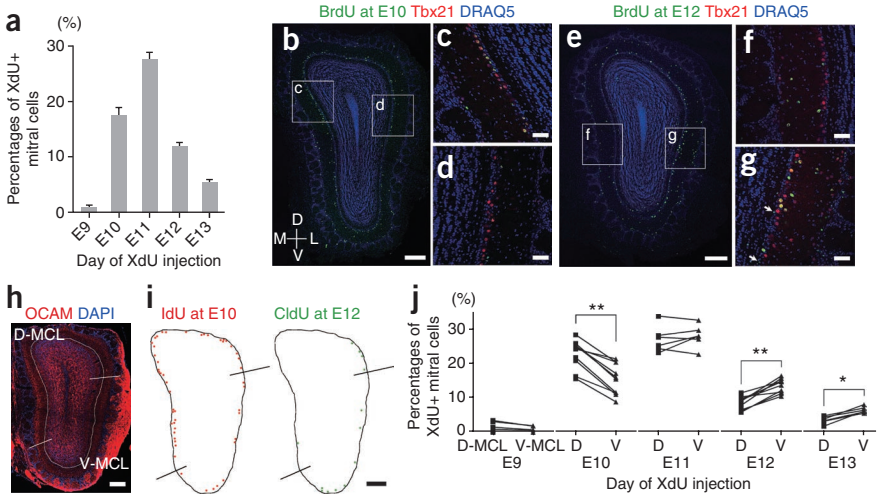

Figure 1 Distributions of mitral cells with different birthdates in the olfactory bulb. (**a**) Percentages of mitral cells in P20 olfactory bulb labeled with thymidine analogs (BrdU, CldU or IdU) injected at indicated time points. (**b**–**g**) Coronal sections of olfactory bulb immunostained with BrdU injected into pregnant dams at E10 (**b**) and E12 (**e**), respectively. More E10-generated (BrdU+; green) mitral cells (Tbx21+; red) were found on the medial (**c**) than lateral side (**d**), whereas E12-generated mitral cells were preferentially located on the lateral side (**f**,**g**). Arrows in **g** indicate BrdU+ Tbx21– cells in the MCL. All cell nuclei are stained with DRAQ5 (blue). (**h**) The MCL was subdivided into dorsomedial (D-) and ventrolateral (V-) MCLs on the basis of OCAM expression in the glomerular layer (red). (**i**) Representative images showing the position of E10- (red) and E12-generated mitral cells (green) labeled with IdU and CldU, respectively, in an olfactory bulb section. (**j**) Percentages of thymidine analog–labeled mitral cells in D- and V-MCLs. Thymidine analogs were applied at indicated time points. Each data point represents a single olfactory bulb, and data obtained from the same olfactory bulb are connected with lines. There were significant differences in distribution between D- and V-MCLs for mitral cells generated at E10 (**$P = 0.002$; $n = 10$ olfactory bulbs), E12 (**$P = 0.002$; $n = 10$) and E13 (*$P = 0.031$; $n = 6$) but not at E9 ($P = 0.125$; $n = 6$) or E11 ($P = 0.563$; $n = 6$; Wilcoxon signed rank test). Error bars, s.e.m. Scale bars, 200 μm (**b**,**e**,**h**,**i**) and 50 μm (**c**,**d**,**f**,**g**).

of the cell cycle. The presence of a copulation plug defined embryonic day (E)0; we injected XdU at E9, 10, 11, 12 or 13. We killed pups at postnatal day (P)20 and immunohistochemically analyzed the XdU-labeling of mitral cells with antibodies to XdU and Tbx21 (**Fig. 1a**–**g**). Around 1, 18, 28, 12 and 6% of mitral cells were labeled when XdU was injected at E9, 10, 11, 12 and 13, respectively (**Fig. 1a**). We also found XdU+ cells, some of which were also Tbx21+, in the external plexiform layer and glomerular layer. These cells were probably tufted cells (Tbx21+) and periglomerular cells (Tbx21–), which are generated shortly after mitral cells with some temporal overlap[26,27]. In addition, we found XdU+ Tbx21– cells in the MCL, especially when we injected XdU at later time points (**Fig. 1g**). These cells are probably a subtype of granule cell that is located in the MCL and generated as early as E12.5 (refs. 27,28).

The majority of E10-generated mitral cells were located in the dorsomedial MCL with fewer in the lateral MCL (**Fig. 1b**–**d**). By contrast, E12-generated mitral cells localized to the ventrolateral region (**Fig. 1e**–**g**). This recalled the dorsal and ventral zone subdivision of the odorant receptor map defined by OCAM expression[29]. Therefore, we subdivided the entire MCL in a coronal slice into dorsomedial (D-MCL) and ventrolateral (V-MCL) regions on the basis of glomerular OCAM expression (**Fig. 1h**). To quantify the distribution of XdU-labeled mitral cells, we calculated the percentages in each subdivision using five coronal slices taken every 400 μm from the anterior to the posterior olfactory bulb (**Fig. 1i** and **Supplementary Fig. 1a**). When we compared the results from the same olfactory bulb, we found that the percentage of E10-generated mitral cells was always higher in D-MCL than V-MCL ($P = 0.002$), whereas there were more E12-generated mitral cells in V-MCL ($P = 0.002$; **Fig. 1j**). MCL maps superimposed with E10- and E12-generated mitral cells revealed the higher density of E10-generated mitral cells in D-MCL than V-MCL, whereas E12-generated mitral cells were denser in V-MCL (**Supplementary Fig. 1b**). The distributions of E9-generated and E13-generated mitral cells were similar to those of E10-generated and E12-generated mitral cells, respectively. There was no significant difference between the D-MCL and V-MCL distributions of E11-generated mitral cells ($P = 0.563$; **Fig. 1j**). These results show that early- and late-generated mitral cells are differentially distributed in the D-MCL and V-MCL.

We also confirmed that the differential distribution of E10-, E11- and E12-generated mitral cells in the P20 olfactory bulb was already present at P0 (**Supplementary Fig. 2**). We found higher percentages of E10-generated mitral cells were found in D-MCL than V-MCL at P0 ($P = 0.008$), whereas there were more E12-generated mitral cells in V-MCL than D-MCL ($P = 0.008$). We found no significant difference in the distribution of E11-generated mitral cells ($P = 0.156$).

Integration of mitral cells into developing olfactory bulb

A possible mechanism for establishing the distinct birthdate-dependent distribution of mitral cells in the MCL is overproduction and subsequent cell death in specific regions. To test this hypothesis, we first investigated whether mitral cells die during embryogenesis. We investigated mitral cell death in E11-generated cells because XdU injections at E11 produced the largest number of labeled mitral cells (**Fig. 1a**). Under these conditions, optimized for detecting mitral cell death by double labeling for cleaved-caspase3 and BrdU, we found no evidence of cell death among E11-generated cells, including mitral cells (**Supplementary Fig. 3**). Moreover, we found at most only a few cleaved-caspase3 positive cells, with or without BrdU labeling, in olfactory bulb slices at any of the ages examined: E11, E12, E13, E14, E15 and E17. We obtained the same results when we measured cell death using a TUNEL assay (**Supplementary Fig. 4**). These results suggest that mitral cells do not die during embryogenesis. Therefore, regardless of their time of origin, cell death is not a determinant of the final localization of mitral cells in the MCL.

An alternative hypothesis is that early- and late-generated mitral cells are fated to integrate specifically into the dorsomedial and ventrolateral portions of the olfactory bulb, respectively. Therefore, we examined the distribution of E10-, E11- and E12-generated mitral cells at E15 (**Fig. 2**). We used Tbr1 to identify mitral cells because not all express Tbx21 at E15. Most E10-generated mitral cells reached the nascent MCL by E15 (**Fig. 2a**,**b**). To quantify their distribution, we divided the olfactory bulb radially into twelve compartments and calculated the percentages of XdU+ and Tbr1+ cells in each compartment (**Fig. 2d**). E10-generated mitral cells were distributed evenly throughout the olfactory bulb, rather than preferentially in the dorsomedial portion (**Fig. 2e**). By contrast, we found more E12-generated

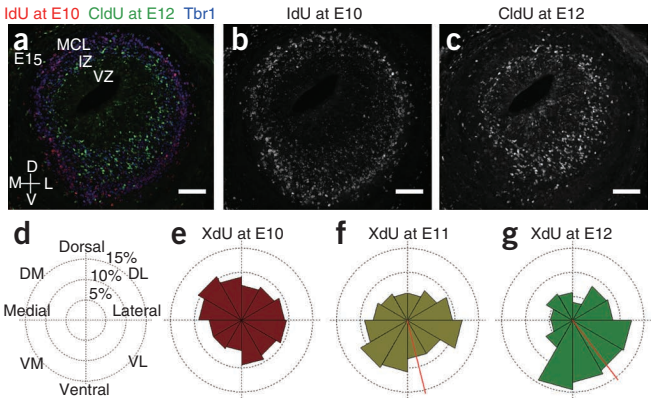

Figure 2 Preferential integration of late-generated mitral cells into the ventrolateral developing olfactory bulb. (**a**) A coronal section of E15 olfactory bulb immunostained with IdU (red), CldU (green) and Tbr1 (blue). (**b**,**c**) Section as in **a** from embryos where IdU (**b**) and CldU (**c**) were injected into pregnant dams at E10 and E12, respectively. E10-generated mitral cells distribute equally throughout the MCL, whereas E12-generated mitral cells are preferentially localized at the ventrolateral portion. IZ, intermediate zone; VZ, ventricular zone. (**d**–**g**) Each olfactory bulb section was radially separated into 12 compartments (**d**) and the percentages of XdU+ Tbr1+ cells found in each compartment among total XdU+ Tbr1+ cells in the section are shown with rose graphs for cells generated at E10 (**e**), E11 (**f**) or E12 (**g**) in E15 olfactory bulb. Thymidine analogs (XdU) were injected at each time point. Six olfactory bulb sections (3 animals) were analyzed for each time point of generation. There is a nonuniform distribution around the circle for E11- ($P < 0.001$) and E12-generated mitral cells ($P < 0.001$) but not for E10-generated mitral cells ($P = 0.258$; Rayleigh test). The population mean angle is shown with a red bar in the graph only when there is a nonuniform distribution. Both E11- ($P < 0.001$) and E12-generated mitral cells ($P < 0.001$) preferentially distributed around the population mean angles (V-test, a modified Rayleigh test). Scale bars, 100 μm.

mitral cells in the ventrolateral portion, although most were in the intermediate zone between the nascent MCL and ventricular zone (**Fig. 2a**,**c**,**g**). E11-generated mitral cells showed a distribution pattern that was intermediate between those of E10- and E12-generated cells (**Fig. 2f**). A Rayleigh test revealed that E10-generated mitral cells were uniformly distributed in the olfactory bulb at E15 ($P = 0.258$). However, the distributions of E11- and E12-generated mitral cells were nonuniform ($P < 0.001$ for both E11 and E12-generated mitral cells). The distribution peaks of both E11- and E12-generated mitral cells were within the ventrolateral portion of the olfactory bulb. These results suggest that late-generated mitral cells preferentially integrate into the ventrolateral portion of the olfactory bulb, whereas early-generated mitral cells do not show a preferential topographic integration. Therefore, the sparse density of E10-generated mitral cells in V-MCL can be attributed to the integration of larger numbers of E11- and E12-generated mitral cells. Likewise, the equal distribution of E11-generated mitral cells in D-MCL and V-MCL found in P20 and P0 olfactory bulbs might reflect the integration of larger numbers of E12-generated mitral cells into V-MCL during continuing embryogenesis.

Tangential migration of mitral cells

What is the underlying mechanism for the specific targeting of late-generated mitral cells to the V-MCL of olfactory bulb? Because mitral cell precursors are first generated in the ventricular zone of the presumptive olfactory bulb[30], we examined whether more mitral cells were generated in the ventrolateral ventricular zone. To test this, we labeled E12-generated cells with BrdU and examined their distributions at E13 and E14. At E13 we found most BrdU+ cells in the ventricular zone (**Fig. 3a**); the nuclei of these cells were radially elongated and parallel to the processes of radial glia (RC2+; **Fig. 3b**), suggesting that they were migrating radially from the ventricular zone toward the intermediate zone. However, we did not find a preferential distribution in the ventrolateral portion. We quantified the distribution as described above, but included all BrdU+ cells in the olfactory bulb because it was too early to use Tbr1 expression to identify E12-generated mitral cells. Despite the nonuniform distribution of E12-generated cells in E13 olfactory bulb ($P < 0.001$), the distribution peak of these cells was in the dorsolateral portion (**Fig. 3c**). At E14, we found many BrdU+ cells with tangentially elongated nuclei in the intermediate zone (**Fig. 3d**,**e**). The distribution peak of E12-generated cells in the olfactory bulb also shifted from dorsolateral to lateral (**Fig. 3f**). Moreover, when we analyzed the distributions of E12-generated cells separately in the anterior and posterior regions of olfactory bulbs at E13 and E14, the percentage of cells in the ventrolateral portion was higher in the posterior than anterior part (**Supplementary Fig. 5**). From these observations, we propose that E12-generated cells migrate tangentially in the intermediate zone toward the postero-ventrolateral region of the olfactory bulb. It was noted previously from Golgi-stained and DiI-labeled tissues that mitral cells in the intermediate zone have a tangential-like morphology[30], but their organization and the underlying reason for the change from radial to tangential were unknown. We suggest that tangentially elongated cells in the intermediate zone are migrating late-generated mitral cells.

To confirm that E12-generated mitral cells have a migratory phenotype, we used DCX-GFP mice in which GFP is expressed under the promoter of doublecortin (DCX), a microtubule-associated protein that is expressed in migrating neurons. We labeled E12-generated cells with BrdU in DCX-GFP mice and then examined GFP expression by Tbr1+ or BrdU+ cells in the olfactory bulb at E14. At this age, there were GFP+ cells at the surface of the olfactory bulb including the intermediate zone and MCL; cells in the ventricular zone were weakly GFP+ (**Fig. 3g**). Most GFP+ cells in the intermediate zone had a tangentially elongated morphology, and both Tbr1+ and BrdU+ cells in this region were GFP+ (**Fig. 3h**). We also found many GFP+ BrdU+ Tbr1+ cells (**Fig. 3h**, asterisks) although not all BrdU+ cells were Tbr1+, and vice versa.

We performed time-lapse imaging to acquire direct evidence for tangential migration in the developing olfactory bulb. We prepared acute slices from the olfactory bulbs of E14 DCX-GFP embryos and imaged GFP+ cells in the intermediate zones every 10 min. We saw many cells migrating tangentially in the intermediate zone. Although migration was not unidirectional, there were cells migrating toward the posterior portion of the olfactory bulb (**Fig. 3i** and **Supplementary Video 1**). After the migration assay, we used Tbr1+ immunohistochemistry to confirm that some tangentially migrating cells were mitral cells (**Fig. 3j**). Consistent with our hypothesis, we also found examples of GFP+ cells that migrated radially (**Supplementary Video 2**) and GFP+ cells that changed orientation from radial to tangential in the E15 olfactory bulb (**Supplementary Video 3**). These results support our hypothesis that late-generated mitral cells migrate tangentially in the intermediate zone of the developing olfactory bulb.

Axons form a migratory scaffold for mitral cells

Radial glial processes support the radial migration of mitral cells in the ventricular zone (**Fig. 3b**). However, it is not known what structure, if any, supports tangential migration. Radial glia also have short

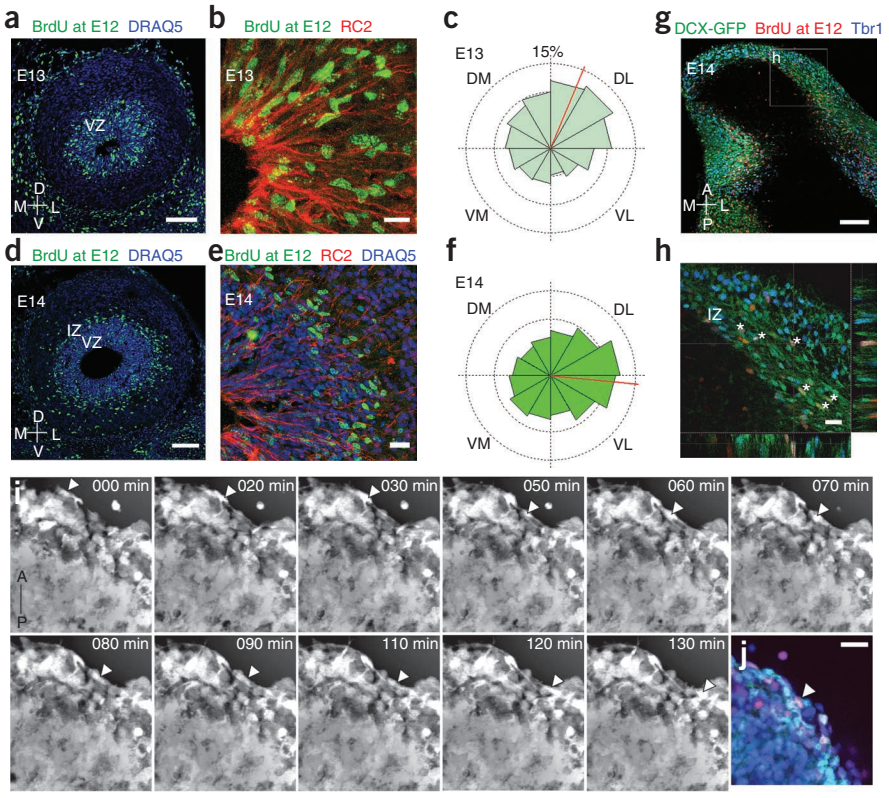

Figure 3 Tangential migration of late-generated mitral cells in the developing olfactory bulb. (**a**,**b**,**d**,**e**) Coronal sections of E13 (**a**,**b**) and E14 (**d**,**e**) olfactory bulbs in which E12-generated cells were labeled with BrdU (green). Radial glial processes were immunostained with RC2 (**b**,**e**; red). (**c**,**f**) Quantification of BrdU+ cell distributions in E13 (**c**) and E14 (**f**) olfactory bulb sections as described in **Figure 2d**. We found a nonuniform distribution of E12-generated cells at both E13 ($P < 0.001$; $n = 6$ olfactory bulbs) and E14 ($P < 0.001$; $n = 6$; Rayleigh test). The population mean angle (red bar) is in the dorsolateral region at E13 but in the lateral region at E14. At both E13 ($P < 0.001$) and E14 ($P < 0.001$), E12-generated cells were preferentially distributed around the population mean angles (V-test). (**g**,**h**) Horizontal section of E14 DCX-GFP mouse olfactory bulb immunostained with BrdU (red) and Tbr1 (blue). BrdU labels E12-generated cells. GFP+ cells in the intermediate zone have a tangentially elongated morphology. BrdU+ or Tbr1+ cells are mostly GFP+, and triple-labeled cells are also found in the slice (**h**, asterisks). (**i**) Time-lapse imaging of acute DCX-GFP E14 mouse olfactory bulb slice to determine the mode of migration of GFP+ cells. A *z*-stack projection was prepared to track cell movement in different planes. The arrowheads show the progression of a GFP+ cell toward the posterior olfactory bulb. (**j**) A single optical slice shows that the GFP+ cell in **i** expresses Tbr1 (red). Scale bars, 100 μm (**a**,**d**,**g**) and 20 μm (**b**,**e**,**h**,**j**).

branches in the intermediate zone of the developing olfactory bulb[31], but it is unlikely that these processes are used for tangential migration; we did not find any evidence of radial glial processes extending tangentially and contacting E12-generated cells within the intermediate zone of the E14 olfactory bulb (**Figs. 3e** and **4a**,**b**). It is possible that these short processes are used for changing migration direction from radial to tangential, but not for sustained tangential migration.

An alternative candidate for mediating tangential migration of late-generated mitral cells is the scaffold formed by the axons of early-generated mitral cells. OCAM is expressed early in developing mitral cells and their axons[32,33]. Therefore, to test for apposition of migrating E12-generated cells and mitral cell axons, we injected BrdU at E12 and stained for OCAM at E14 (**Fig. 4c**–**f**). We found mitral cell axons running toward the lateral and posterior intermediate zone in both coronal (**Fig. 4c**)

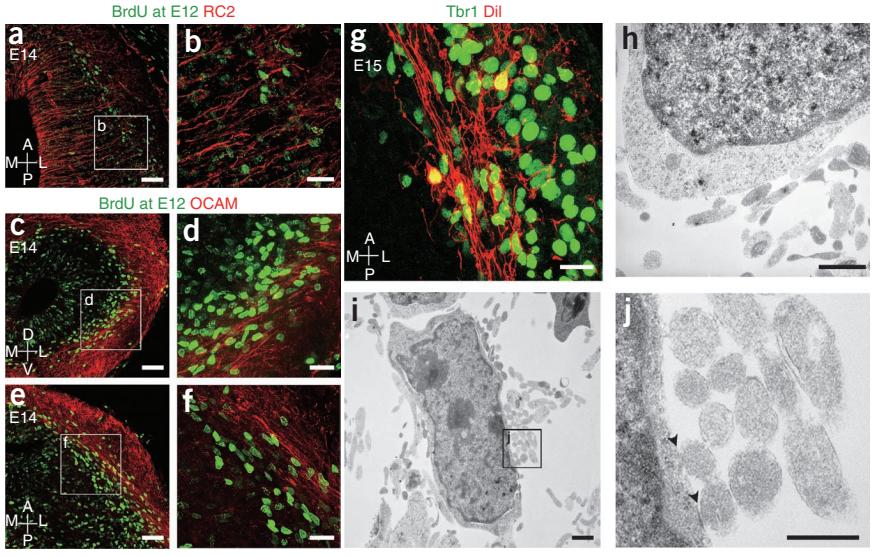

Figure 4 Direct contact of E12-generated mitral cells with pre-existing mitral cell axons. (**a**,**b**) Horizontal section of an E14 olfactory bulb immunostained with BrdU (green, E12-generated cells) and RC2 (red). RC2+ processes do not run tangentially in the olfactory bulb. (**c**–**f**) Coronal (**c**,**d**) and horizontal (**e**,**f**) sections of E14 olfactory bulb immunostained with BrdU (green, E12-generated cells) and OCAM (red), which labels mitral cell axons. Mitral cell axons run tangentially in the intermediate zone and contact tangentially elongated BrdU+ cells. (**g**) Horizontal section of an E15 olfactory bulb. Mitral cell axons were labeled with DiI (red) injected into the lateral olfactory tract, and the nuclei of mitral cells were immunostained with Tbr1 (green). Pre-existing mitral cell axons pass the intermediate zone, which contains many mitral cells that have tangentially elongated morphology. (**h**–**j**) Electron microscopic images of E15 olfactory bulbs. Electron-dense products were produced in nuclei of Tbr1+ cells with a DAB reaction. Tbr1+ cells with elongated nuclei are surrounded by many axons (**h**,**i**), and some axons make direct contacts with Tbr1+ cells (**j**; arrowheads). Scale bars, 50 μm (**a**,**c**,**e**), 20 μm (**b**,**d**,**f**,**g**), 1 μm (**h**,**i**) and 500 nm (**j**).

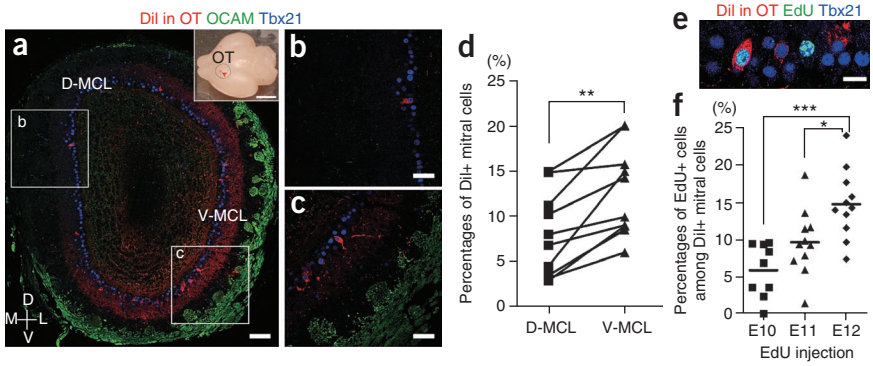

Figure 5 Birthdate-regulated axonal projection to the olfactory tubercle. (**a**–**c**) Coronal section of P5 olfactory bulb. A subpopulation of mitral cells was labeled with DiI injected into the olfactory tubercle (OT); arrowhead in inset shows injection site. Many DiI+ (red) mitral cells (Tbx21+; blue) are found in the ventrolateral portion (**c**) but there are fewer DiI+ mitral cells in the dorsomedial portion (**b**). (**d**) The MCL in olfactory bulb sections was subdivided into D- and V-MCLs on the basis of OCAM expression in the glomerular layer (green in **a**) and the percentages of DiI+ mitral cells were quantified in each zone. A significantly higher percentage of mitral cells were DiI+ in the V-MCL than in the D-MCL (**$P = 0.002$; $n = 10$ olfactory bulbs; Wilcoxon signed rank test). (**e**) Detection of mitral cells projecting to the olfactory tubercle generated at specific time points in development. EdU injected at E12 was detected (green) in mitral cells (Tbx21+; blue) after DiI (red) injection into the olfactory tubercle at P5. (**f**) Percentages of EdU+ cells among mitral cells projecting to the olfactory tubercle (DiI+) were quantified after injecting EdU at E10, E11 or E12. The percentage was higher when EdU was injected at E12 ($n = 11$ olfactory bulbs) than E10 ($n = 9$) or E11 ($n = 11$). *$P < 0.05$; ***$P < 0.001$; one-way ANOVA followed by Tukey's multiple comparison test. Scale bars, 100 μm (**a**), 2 mm (inset in **a**), 50 μm (**b**,**c**) and 20 μm (**e**).

and horizontal sections (**Fig. 4e**). The tangentially elongated E12-generated cells were positioned in parallel with, and closely apposed to, the OCAM+ axons (**Fig. 4d**,**f**). As a further test, we labeled the axons with DiI injections into the lateral olfactory tract and labeled the nuclei of mitral cells with Tbr1 staining at E15. Consistently, the tangentially elongated mitral cells (Tbr1+) were closely aligned with DiI+ axons of earlier-generated mitral cells (**Fig. 4g**). We then used immunoelectron microscopy to determine whether the Tbr1+ cells were in direct contact with axons. At E15 mitral cells, we identified Tbr1+ cells by the electron-dense DAB reaction in their nuclei and their elongated tangential morphology in horizontal sections. These cells were typically surrounded by large numbers of axons (**Fig. 4h**,**i**), many of which formed somato-axonal appositions (**Fig. 4j**, arrowheads).

We observed tangentially elongated BrdU+ and Tbr1+ cells in the intermediate zone only at E14 and E15. At these time points, the axons of early-born mitral cells are probably the only fibrous structure in this region[34], other than the short branches of radial glia. An alternative mechanism for mitral cell migration is the chain migration that is used by olfactory interneurons in the rostral migratory stream. However, we think this is unlikely because we did not observe the dense packing that is typical of this chain migration[35]. Thus, the axons of early-generated mitral cells are the most plausible structure to provide a scaffold to support the tangential migration of late-generated mitral cells toward the postero-ventro-lateral developing olfactory bulb. This adds further support to our initial finding of the differential distribution of early- versus late-generated mitral cells in the olfactory bulb, and is consistent with prior reports that the lateral olfactory tract is first formed by mitral cells in the medial olfactory bulb[36].

Differential mitral cell projection to olfactory tubercle

It has been suggested that the olfactory tubercle receives more axons from mitral cells in the ventral olfactory bulb[21,22]. We injected DiI into the P5 olfactory tubercle and examined the distribution of labeled mitral cells in the olfactory bulb (**Fig. 5a**). Although we found labeled mitral cells throughout the MCL, consistent with the previous studies, we found larger numbers of DiI+ mitral cells in the ventrolateral region (**Fig. 5a**). In addition, DiI staining in the external plexiform layer, where the secondary dendrites of mitral cells extend, was more intense in the ventrolateral than in the dorsomedial olfactory bulb (**Fig. 5b**,**c**). For comparison with the odorant receptor map, we subdivided the MCL into D-MCL and V-MCL on the basis of glomerular OCAM expression and quantified the percentages of DiI+ mitral cells (**Fig. 5d**). Because DiI volumes and injection sites in the olfactory tubercle varied between animals, the percentages were variable. Nevertheless, the density of mitral cells that projected to the olfactory tubercle was significantly greater in V-MCL than in D-MCL ($P = 0.002$).

As the distribution of mitral cells that projected to the olfactory tubercle in the MCL was similar to that of E12-generated mitral cells, we investigated whether mitral cells with different birthdates differed in their axonal projections to the olfactory tubercle. We used another thymidine analog, 5-ethynyl-2′-deoxyuridine (EdU), to label mitral cells because EdU detection is compatible with DiI[37] (**Fig. 5e**). After injecting EdU at E10, 11 or 12, we placed DiI into the olfactory tubercle at P5 and determined the percentages of DiI and EdU double-labeled mitral cells (**Fig. 5f**). A significantly higher percentage of DiI+ mitral cells were co-labeled with EdU injected at E12 compared to E10 ($P < 0.001$) or E11 ($P < 0.05$). Thus, the olfactory tubercle receives a heavier axonal projection from late-generated than early-generated mitral cells. This indicates that the asymmetrical distribution of mitral cells that innervate the olfactory tubercle depends on their birthdates.

DISCUSSION

In the mammalian neocortex the laminar and areal positions of pyramidal neurons, which ultimately determine their connectivity and function, are directly correlated with the time of their origin[24,25]. In contrast to the cortical multilayer cellular organization, mitral cells in the olfactory bulb are aligned in single layer, and had not been previously evaluated for segregation into subpopulations based on the timing of their last cell division. Here, we show that mitral cells that have different birthdates are differentially distributed in the MCL and that the late-generated mitral cells extend stronger projections to the olfactory tubercle than the early-generated cells. Our data suggest that, like cerebral cortex[24], the birthdates of mitral cells in the olfactory system might determine their segregation into spatially and functionally defined subpopulations. Thus, we propose the existence of two topographically defined maps in the olfactory bulb that interface at the glomeruli. Map 1 (odorant receptor map) is the glomerular distribution of olfactory sensory neuron axons according to odorant receptor expression. Map 2 (mitral cell map) represents the birthdate-dependent location of the mitral cells in the olfactory bulb. Considering the zonal segregation of the odorant receptor map[29] and the columnar structure constructed by granule cells in the olfactory bulb[38], the formation of the mitral cell

map might provide a fundamental framework by which mitral cells decode the signal from olfactory sensory neurons.

Development of the olfactory bulb

The time-course of development is not uniform throughout the olfactory bulb. For example, glomeruli are reported to appear first in the antero-dorsal region of developing olfactory bulb[39], although synaptogenesis in the glomerular layer occurs earlier in the ventral region[40]. More recently, it was shown that all cells that express Pcdh21, a mitral cell marker, at E14 were positive for OCAM[41]. Among mitral cells, OCAM is expressed only by those in the dorsomedial region of the olfactory bulb[33], indicating that mitral cells in the dorsomedial region mature earlier than other mitral cells. Thus, olfactory bulb development might begin dorsomedially and then expand to the ventrolateral olfactory bulb. Our finding that there is a differential distribution of early- and late-generated mitral cells in D-MCL and V-MCL also supports this perspective, although the segregation was not exclusive.

Here we also propose that tangential migration of late-generated mitral cells along a scaffold of axons from early-generated mitral cells is an underlying cellular mechanism for generating a dorsomedial-ventrolateral gradient of mitral cell development (**Supplementary Fig. 6**). Elucidating the molecular mechanisms that regulate the migration and detachment of migrating mitral cells from the axonal scaffold in the posterior olfactory bulb will give us better insight into spatial and temporal differences in olfactory bulb development.

Mitral cell location, projection and birthdates

We found significant differences in the distribution of E10- and E12-generated mitral cells when we subdivided the MCL into dorsomedial and ventrolateral regions on the basis of glomerular OCAM expression. Because olfactory sensory neurons that target the dorsal and ventral zones make synapses primarily with mitral cells in the D-MCL and V-MCL, respectively, odor information from dorsal zone olfactory sensory neurons is processed largely by early-generated mitral cells and that from ventral zone olfactory sensory neurons is processed largely by late-generated mitral cells. The segregation of early- and late-generated mitral cells into D-MCL and V-MCL is not an all-or-none event. In both domains early- and late-generated cells are slightly intermingled. Although this provides both early- and late-generated mitral cells with an opportunity to process odor information from dorsal and ventral zone olfactory sensory neurons, the ratios are profoundly different. Thus, the distinct locations of mitral cells with different birthdates may contribute to functional specificity of the different zones of the odorant receptor map[10].

We have also shown that the olfactory tubercle receives more axons from E12-generated mitral cells than from those generated at E10 or E11. In rabbits, approximately one-fourth of the mitral cells in the ventral olfactory bulb send their axons to the olfactory tubercle[42]. Our data suggest that the axonal projection of mitral cells to the olfactory tubercle is partly determined by their birthdates. A similar correlation has been observed during the genesis of tufted cells, which are born later than mitral cells[26] and project predominately to the olfactory tubercle[21,43,44]. Moreover, we propose that mitral cells generated at different time points send their axons to spatially distinct regions in the olfactory cortex. As early- and late-generated mitral cells send their axons through different sub-laminae in the lateral olfactory tract[32], mitral cell axons that target different regions of the olfactory cortices may begin to segregate in the lateral olfactory tract. Together with studies of molecular mechanisms that regulate the organization of the lateral olfactory tract and axonal topography in olfactory cortices[45–47], studies that focus on the birthdates of mitral or tufted cells might uncover rules that link the olfactory bulb and the olfactory cortices.

In summary, our results show that both the locations of mitral cell somata in the MCL and the extent of their axonal projections in the olfactory cortices are in part a function of their date of birth. Considering that the spatial distribution of mitral cells with different birthdates correlates systematically with the dorsal and ventral zones of the odorant receptor map, it is likely that processing of distinct odors in the olfactory cortices depends on the information flow from the dorsal and ventral zones of the odorant receptor map. Thus, our data suggest a developmental mechanism that may be used by the olfactory bulb projection neurons to organize the transmission of information from the odorant receptor map to the olfactory cortices. The physiological significance of an odorant receptor map for information processing in the olfactory cortices is still largely unknown. Also, our data show that although there is a significant difference in cortical projection based on date of birth, it is not exclusive pattern of projections; there is evidence for some intermingling of early- and late-generated mitral cells. Nevertheless, our data show that there is a developmental gradient in mitral cell location and connections, characteristics that will be useful as we continue to unravel the rules that regulate odor processing.

METHODS

Methods and any associated references are available in the online version of the paper at http://www.nature.com/natureneuroscience/.

Note: Supplementary information is available on the Nature Neuroscience website.

ACKNOWLEDGMENTS

We thank K. Mori for the antibody to OCAM, Y. Yoshihara for the antibody to Tbx21, A. Bordey for the DCX-GFP mice and all of the members of the Greer, Rakic and Treloar laboratories for technical assistance and discussion. The antibody to RC2 developed by M. Yamamoto was obtained from the Developmental Studies Hybridoma Bank developed under the auspices of the US National Institute of Child Health and Human Development and maintained by the Department of Biology, University of Iowa. This work was supported by the US National Institute of Health and the Kavli Institute for Neuroscience at Yale.

AUTHOR CONTRIBUTIONS

F.I. and C.A.G. designed the study, analyzed data and wrote the manuscript. F.I. conducted the experiments. Time-lapse live imaging was done by F.I. and A.E.A. F.I., C.A.G., A.E.A. and P.R. discussed the results and commented on the manuscript.

COMPETING FINANCIAL INTERESTS

The authors declare no competing financial interests.

Published online at http://www.nature.com/natureneuroscience/.
Reprints and permissions information is available online at http://npg.nature.com/reprintsandpermissions/.

1. Vassar, R. *et al.* Topographic organization of sensory projections to the olfactory bulb. *Cell* **79**, 981–991 (1994).
2. Ressler, K.J., Sullivan, S.L. & Buck, L.B. Information coding in the olfactory system: evidence for a stereotyped and highly organized epitope map in the olfactory bulb. *Cell* **79**, 1245–1255 (1994).
3. Mombaerts, P. *et al.* Visualizing an olfactory sensory map. *Cell* **87**, 675–686 (1996).
4. Mori, K., Nagao, H. & Yoshihara, Y. The olfactory bulb: coding and processing of odor molecule information. *Science* **286**, 711–715 (1999).
5. Imai, T. & Sakano, H. Odorant receptor–mediated signaling in the mouse. *Curr. Opin. Neurobiol.* **18**, 251–260 (2008).
6. Kaneko-Goto, T., Yoshihara, S., Miyazaki, H. & Yoshihara, Y. BIG-2 mediates olfactory axon convergence to target glomeruli. *Neuron* **57**, 834–846 (2008).
7. Serizawa, S. *et al.* A neuronal identity code for the odorant receptor–specific and activity-dependent axon sorting. *Cell* **127**, 1057–1069 (2006).
8. Imai, T. *et al.* Pre-target axon sorting establishes the neural map topography. *Science* **325**, 585–590 (2009).
9. Imai, T., Suzuki, M. & Sakano, H. Odorant receptor–derived cAMP signals direct axonal targeting. *Science* **314**, 657–661 (2006).

10. Kobayakawa, K. *et al.* Innate versus learned odour processing in the mouse olfactory bulb. *Nature* **450**, 503–508 (2007).
11. Bozza, T. *et al.* Mapping of class I and class II odorant receptors to glomerular domains by two distinct types of olfactory sensory neurons in the mouse. *Neuron* **61**, 220–233 (2009).
12. Mori, K., Takahashi, Y.K., Igarashi, K.M. & Yamaguchi, M. Maps of odorant molecular features in the mammalian olfactory bulb. *Physiol. Rev.* **86**, 409–433 (2006).
13. Johnson, B.A. & Leon, M. Chemotopic odorant coding in a mammalian olfactory system. *J. Comp. Neurol.* **503**, 1–34 (2007).
14. Matsumoto, H. *et al.* Spatial arrangement of glomerular molecular-feature clusters in the odorant-receptor class domains of the mouse olfactory bulb. *J. Neurophysiol.* **103**, 3490–3500 (2010).
15. Soucy, E.R., Albeanu, D.F., Fantana, A.L., Murthy, V.N. & Meister, M. Precision and diversity in an odor map on the olfactory bulb. *Nat. Neurosci.* **12**, 210–220 (2009).
16. Johnson, B.A., Xu, Z., Ali, S.S. & Leon, M. Spatial representations of odorants in olfactory bulbs of rats and mice: similarities and differences in chemotopic organization. *J. Comp. Neurol.* **514**, 658–673 (2009).
17. Poo, C. & Isaacson, J.S. Odor representations in olfactory cortex: "sparse" coding, global inhibition, and oscillations. *Neuron* **62**, 850–861 (2009).
18. Stettler, D.D. & Axel, R. Representations of odor in the piriform cortex. *Neuron* **63**, 854–864 (2009).
19. Murthy, M., Fiete, I. & Laurent, G. Testing odor response stereotypy in the *Drosophila* mushroom body. *Neuron* **59**, 1009–1023 (2008).
20. Miyasaka, N. *et al.* From the olfactory bulb to higher brain centers: genetic visualization of secondary olfactory pathways in zebrafish. *J. Neurosci.* **29**, 4756–4767 (2009).
21. Scott, J.W., McBride, R.L. & Schneider, S.P. The organization of projections from the olfactory bulb to the piriform cortex and olfactory tubercle in the rat. *J. Comp. Neurol.* **194**, 519–534 (1980).
22. Haberly, L.B. & Price, J.L. The axonal projection patterns of the mitral and tufted cells of the olfactory bulb in the rat. *Brain Res.* **129**, 152–157 (1977).
23. Jefferis, G.S., Marin, E.C., Stocker, R.F. & Luo, L. Target neuron prespecification in the olfactory map of *Drosophila*. *Nature* **414**, 204–208 (2001).
24. Rakic, P., Ayoub, A.E., Breunig, J.J. & Dominguez, M.H. Decision by division: making cortical maps. *Trends Neurosci.* **32**, 291–301 (2009).
25. Molyneaux, B.J., Arlotta, P., Menezes, J.R. & Macklis, J.D. Neuronal subtype specification in the cerebral cortex. *Nat. Rev. Neurosci.* **8**, 427–437 (2007).
26. Hinds, J.W. Autoradiographic study of histogenesis in the mouse olfactory bulb. I. Time of origin of neurons and neuroglia. *J. Comp. Neurol.* **134**, 287–304 (1968).
27. Batista-Brito, R., Close, J., Machold, R. & Fishell, G. The distinct temporal origins of olfactory bulb interneuron subtypes. *J. Neurosci.* **28**, 3966–3975 (2008).
28. Imamura, F. *et al.* A leucine-rich repeat membrane protein, 5T4, is expressed by a subtype of granule cells with dendritic arbors in specific strata of the mouse olfactory bulb. *J. Comp. Neurol.* **495**, 754–768 (2006).
29. Mori, K., von Campenhause, H. & Yoshihara, Y. Zonal organization of the mammalian main and accessory olfactory systems. *Phil. Trans. R. Soc. Lond. B* **355**, 1801–1812 (2000).
30. Blanchart, A., De Carlos, J.A. & Lopez-Mascaraque, L. Time frame of mitral cell development in the mice olfactory bulb. *J. Comp. Neurol.* **496**, 529–543 (2006).
31. Puche, A.C. & Shipley, M.T. Radial glia development in the mouse olfactory bulb. *J. Comp. Neurol.* **434**, 1–12 (2001).
32. Inaki, K., Nishimura, S., Nakashiba, T., Itohara, S. & Yoshihara, Y. Laminar organization of the developing lateral olfactory tract revealed by differential expression of cell recognition molecules. *J. Comp. Neurol.* **479**, 243–256 (2004).
33. Treloar, H.B., Gabeau, D., Yoshihara, Y., Mori, K. & Greer, C.A. Inverse expression of olfactory cell adhesion molecule in a subset of olfactory axons and a subset of mitral/tufted cells in the developing rat main olfactory bulb. *J. Comp. Neurol.* **458**, 389–403 (2003).
34. Hinds, J.W. Early neuron differentiation in the mouse olfactory bulb. II. Electron microscopy. *J. Comp. Neurol.* **146**, 253–276 (1972).
35. Lois, C., Garcia-Verdugo, J.M. & Alvarez-Buylla, A. Chain migration of neuronal precursors. *Science* **271**, 978–981 (1996).
36. Grafe, M.R. & Leonard, C.M. Developmental changes in the topographical distribution of cells contributing to the lateral olfactory tract. *Brain Res.* **255**, 387–400 (1982).
37. Salic, A. & Mitchison, T.J. A chemical method for fast and sensitive detection of DNA synthesis *in vivo*. *Proc. Natl. Acad. Sci. USA* **105**, 2415–2420 (2008).
38. Willhite, D.C. *et al.* Viral tracing identifies distributed columnar organization in the olfactory bulb. *Proc. Natl. Acad. Sci. USA* **103**, 12592–12597 (2006).
39. Bailey, M.S., Puche, A.C. & Shipley, M.T. Development of the olfactory bulb: evidence for glia-neuron interactions in glomerular formation. *J. Comp. Neurol.* **415**, 423–448 (1999).
40. Blanchart, A., Romaguera, M., Garcia-Verdugo, J.M., de Carlos, J.A. & Lopez-Mascaraque, L. Synaptogenesis in the mouse olfactory bulb during glomerulus development. *Eur. J. Neurosci.* **27**, 2838–2846 (2008).
41. Takeuchi, H. *et al.* Sequential arrival and graded secretion of Sema3F by olfactory neuron axons specify map topography at the bulb. *Cell* **141**, 1056–1067 (2010).
42. Ojima, H., Mori, K. & Kishi, K. The trajectory of mitral cell axons in the rabbit olfactory cortex revealed by intracellular HRP injection. *J. Comp. Neurol.* **230**, 77–87 (1984).
43. Scott, J.W. Electrophysiological identification of mitral and tufted cells and distributions of their axons in olfactory system of the rat. *J. Neurophysiol.* **46**, 918–931 (1981).
44. Nagayama, S. *et al.* Differential axonal projection of mitral and tufted cells in the mouse main olfactory system. *Front. Neural Circuits* **4**, 120 (2010).
45. Hirata, T. & Fujisawa, H. Environmental control of collateral branching and target invasion of mitral cell axons during development. *J. Neurobiol.* **38**, 93–104 (1999).
46. Fouquet, C. *et al.* Robo1 and robo2 control the development of the lateral olfactory tract. *J. Neurosci.* **27**, 3037–3045 (2007).
47. Soussi-Yanicostas, N. *et al.* Anosmin-1, defective in the X-linked form of Kallmann syndrome, promotes axonal branch formation from olfactory bulb output neurons. *Cell* **109**, 217–228 (2002).

ONLINE METHODS

Animals. All the experiments were performed in mice. Unless noted, we used the CD-1 mouse strain (Charles River Laboratories) as the wild type. DCX-GFP mice (GENSAT BAC transgenic, strain name STOCK Tg(Dcx-EGFP)1Gsat/Mmmh) were a gift from A. Bordey (Yale University). The day on which we found a copulation plug was called E0, and the succeeding days of gestation were numbered in order. Intraperitoneal injections of thymidine analogs (BrdU, CldU, IdU or EdU) into pregnant dams (50 mg kg^{-1}) were performed once between 10 am and noon. Prenatal embryos were harvested and fixed in 4% paraformaldehyde (PFA, wt/vol) overnight after thymidine analog–injected dams were killed by CO_2 inhalation. P0 and P5 pups were killed by CO_2 inhalation and the brains were fixed in 4% PFA overnight. P20 mice were anesthetized with pentobarbital and perfused transcardially with phosphate-buffered saline (PBS) with 1 unit per ml heparin, followed by 4% PFA. The brain was removed from the skull and postfixed in the same fixative for 2 h. All animal care and use was approved by the Yale University Animal Care and Use Committee.

DiI staining. To label mitral cells in the fixed olfactory bulb, glass micropipettes filled with 6% DiI (1, 1′-dioctadecyl-3, 3, 3′3′-tetramethylindocarbocyanine perchlorate, wt/vol; Sigma) dissolved in dimethylformamide were inserted into the lateral olfactory tract of E15 or the olfactory tubercle of P5 brains to leave small amount of DiI solution (<500 nl) in the tissue. Then, the brains were incubated in PBS at 37 °C until use. The olfactory bulbs were cut on a vibratome (50–100 µm) and cells labeled with DiI were visualized by fluorescence microscopy.

Immunohistochemistry. For cryosectioned slices, the fixed brains were cryopreserved in 30% sucrose (wt/vol) in 0.1 M phosphate buffer (pH 7.4), and embedded in optimal cutting temperature compound (Sakura Finetek). The olfactory tissues were cut on a cryostat into 20-µm slices and stored at −20 °C until use. The slices were first rinsed with TBS-T (10 mM Tris-HCl (pH 7.4), 100 mM NaCl with 0.3% Triton-X100 (vol/vol)), blocked with blocking buffer (3% bovine serum albumin (BSA, wt/vol) and 5% normal donkey serum (vol/vol) in TBS-T) at 20–25 °C for 1 h and incubated with primary antibodies diluted in blocking buffer overnight at 20–25 °C or 4 °C. Sections were washed with TBS-T, then incubated with secondary antibodies with 4′6-diamino-2-phenylindole dihydrochrolide (DAPI; Invitrogen) or DRAQ5 (Biostatus Ltd.) for nucleus staining for 1 h. The immunoreacted sections were washed and mounted with Gel/Mount mounting medium (Biomeda).

For vibratome-sectioned slices, the fixed brains were cut with a vibratome into 50-µm slices and stored in PBS at 4 °C until use. PBS-T was used instead of TBS-T and sections were incubated in blocking buffer and secondary antibodies for 2 h. For DiI-stained slices identical steps were performed without Triton-X100.

To detect BrdU, CldU or IdU (Sigma), the slices were pre-treated for 30 min in 0.025 M HCl at 65 °C for cryosectioned slices or 2 M HCl at 37 °C for vibratome-sectioned slices, and rinsed with 0.1 M borate buffer (pH 8.5)[48] before the steps described above. EdU (Invitrogen) was detected as described[37]. Briefly, the olfactory bulb slices were stained by incubating for 30 min with 100 mM Tris-HCl (pH 8.5), 1 mM CuSO4, 100 mM ascorbic acid and 10 mg ml^{-1} Alexa Fluor 488 azide (Invitrogen).

For primary antibodies, we used rat antibody to BrdU/CldU (1:100; Accurate Chemical & Scientific Corporation), mouse antibody to BrdU/IdU (1:200; BD Biosciences), rabbit antibody to OCAM (1:2,000; provided by K. Mori, University of Tokyo), rabbit antibody to cleaved caspase3 (1:100; Cell Signaling Technology), rabbit and guinea pig antibody to Tbx21 (1:20,000; provided by Y. Yoshihara, RIKEN), rabbit antibody to Tbr1 (1:10,000; Millipore), and mouse RC2 (1:5; Developmental Studies Hybridoma Bank). Goat or donkey anti-species IgG conjugated with Alexa 488, Alexa 555, Alexa 674 (Invitrogen), Cy2, Cy3 or Cy5 (Jackson Immunochemicals) were used as secondary antibodies.

TUNEL assay. The cryosectioned slices were used for the TUNEL assay. The NeuroTACS II kit (Trevigen Inc.) was used according to the manufacturer's directions, except it was developed with streptavidin-Alexa 488 rather than HRP and DAB, and the tissue was counterstained with DRAQ5.

Electron microscopy. The mouse embryos were fixed with 4% PFA and 0.2% glutaraldehyde (vol/vol) overnight. Brains were rinsed in PBS overnight and cut on a vibratome (50 µm). The sections were blocked in 3% BSA and 5% normal donkey serum at 20–25 °C for 2 h and incubated with primary antibody for two nights at 4 °C. Biotinylated secondary antibody was followed by the ABC reagent (Vector) and a DAB peroxidase reaction. Tissue was then counterstained with osmium tetroxide and embedded for thin sectioning in acrylite. Sections of 100 nm were examined on a JEOL transmission electron microscope (JEOL USA) and photographed at 4,000–15,000× primary magnification.

Multiphoton live imaging. Imaging was performed on a LSM510 META (Carl Zeiss) coupled to a Chameleon-Ultra laser (Coherent) tuned to 900 nm to excite EGFP. Slices of E14 or E15 olfactory bulbs were moved to a RC40 recording chamber (Warner Instruments), maintained at 37 °C and constantly perfused with slice culture medium as described[49]. *Z*-stacks were collected every 10 min and analysis was carried out using Zen 2009 (Carl Zeiss).

Image acquisition and statistical analysis. To count the thymidine analog-labeled mitral cells in P0 and P20 olfactory bulb slices, images of five coronal slices taken every 400 µm from anterior to posterior (**Supplementary Fig. 1a**) were acquired using a fluorescent microscope (BX51, Olympus Corporation) with 20× objectives. Levels were adjusted in Photoshop software (Adobe), but the images were otherwise unaltered. The numbers of thymidine analog–labeled cells and mitral cells in the MCL were manually counted and percentages of mitral cells labeled with thymidine analog were calculated. Images acquired with a laser scanning confocal microscope (Leica TCS SL) with 20× or 40× objectives were used to analyze the distribution of thymidine analog–labeled cells in the embryonic olfactory bulb. To compare the distributions of E12-generated cells between anterior and posterior olfactory bulbs at E13 and E14, two coronal sections 100 µm apart were obtained from a single olfactory bulb (**Supplementary Fig. 5**). The numbers of thymidine analog–labeled cells in each compartment of the olfactory bulb slices were manually counted and the percentages for radar charts were calculated by dividing numbers in each compartment by the total number in the slice. To analyze the distribution of DiI-labeled olfactory tubercle–projecting mitral cells in the olfactory bulb, images were acquired with a laser scanning confocal microscope with 20× objective. The numbers of mitral cells and DiI-labeled mitral cells in the MCL were manually counted and percentages of mitral cells labeled with DiI were calculated. The percentages of mitral cells labeled with EdU, injected at E10, E11 or E12, were manually calculated using confocal images taken with 40× objective. Statistical analyses except for circular statistics were performed using GraphPad Prism 4 software (GraphPad Software). Circular statistics were performed using Oriana software (Kovach Computing Services).

48. Yamaguchi, M. & Mori, K. Critical period for sensory experience-dependent survival of newly generated granule cells in the adult mouse olfactory bulb. *Proc. Natl. Acad. Sci. USA* **102**, 9697–9702 (2005).
49. Burns, K.A. *et al.* Nestin-CreER mice reveal DNA synthesis by nonapoptotic neurons following cerebral ischemia hypoxia. *Cereb. Cortex* **17**, 2585–2592 (2007).

doi:10.1038/nn.2754

Transcriptional programs in transient embryonic zones of the cerebral cortex defined by high-resolution mRNA sequencing

Albert E. Ayoub[a], Sunghee Oh[b], Yanhua Xie[a], Jing Leng[b,c], Justin Cotney[b], Martin H. Dominguez[a], James P. Noonan[b,c,d], and Pasko Rakic[a,d,1]

Departments of [a]Neurobiology and [b]Genetics, Yale University School of Medicine, New Haven, CT 06520; and [c]Program in Computational Biology and Bioinformatics and [d]Kavli Institute for Neuroscience, Yale University, New Haven, CT 06520

Contributed by Pasko Rakic, August 1, 2011 (sent for review June 20, 2011)

Characterizing the genetic programs that specify development and evolution of the cerebral cortex is a central challenge in neuroscience. Stem cells in the transient embryonic ventricular and subventricular zones generate neurons that migrate across the intermediate zone to the overlying cortical plate, where they differentiate and form the neocortex. It is clear that not one but a multitude of molecular pathways are necessary to progress through each cellular milestone, yet the underlying transcriptional programs remain unknown. Here, we apply differential transcriptome analysis on microscopically isolated cell populations, to define five transcriptional programs that represent each transient embryonic zone and the progression between these zones. The five transcriptional programs contain largely uncharacterized genes in addition to transcripts necessary for stem cell maintenance, neurogenesis, migration, and differentiation. Additionally, we found intergenic transcriptionally active regions that possibly encode unique zone-specific transcripts. Finally, we present a high-resolution transcriptome map of transient zones in the embryonic mouse forebrain.

radial glia | pyramidal neurons | cortical development | laser microdissection

One of the main characteristics of the developing neocortex is the generation of various cellular zones, most of which begin to disappear by late gestation (1, 2). During corticogenesis, progenitor cells in the ventricular zone undergo two distinct modes of division (3, 4). Symmetric divisions expand the surface area of the cortex by increasing the number of progenitors, whereas asymmetric divisions produce intermediate progenitors (INPs) or postmitotic neurons (PNs) that pass through the subventricular zone (SVZ) and intermediate zone (IZ), respectively (5, 6). These newly generated daughter cells then produce the outermost zone, the cortical plate (CP), where neurons align in an inside-out pattern to form the six-layered cerebral cortex. Recent studies highlight the dependence of normal corticogenesis on genetic programs involving a multitude of genes and that the disruption of these genetic programs is thought to cause the majority of brain disorders and malformations (7–9).

Significant progress in developmental neuroscience has often been tied to technological breakthroughs and creative use of sophisticated techniques (10). The past decade witnessed significant advances in the developmental neuroscience field as a result of the increasing adoption of genome-wide approaches. For example, global analyses of gene expression with the use of microarrays have identified genes involved in progenitor cell proliferation (11) and specification of cortical layers (12, 13). Although several studies have divided the developing brain into functional areas to study arealization (14, 15) and gene networks (16), to date we are aware of no study that has determined the full repertoire of transcripts necessary for the progression of cells from birth to differentiation.

Whole-transcriptome mRNA sequencing (mRNA-seq) is a breakthrough technology that provides quantitative and sensitive detection with a broad dynamic range (17), which was recently demonstrated by Han and colleagues (18). This study described global gene and alternative isoform expression using mRNA-seq on mouse neocortex at late embryonic (embryonic day [E] 18) and early postnatal (postnatal day [P] 7) ages. It became clear that overcoming limits in spatial resolution is a necessary step to determine transcriptional programs that define the maintenance of neural stem cells in the VZ, the migration of neurons through the SVZ–IZ, and finally the differentiation of neurons in the CP. Therefore, we performed differential expression analysis after mRNA-seq on cells collected by laser microdissection (LMD) from each transient embryonic zone. We characterized the full repertoire of zone-specific transcribed genes, alternative isoforms, and novel transcriptionally active regions (nTAR) at a level of resolution that has not, to the best of our knowledge, been previously achieved. By using this approach, we were able to expose genetic programs that define milestones of corticogenesis.

Results

High-Resolution Differential Gene Expression. Resolving expression differences among small cellular groups and detecting genes expressed at low levels are common limitations of whole-cortex studies. To overcome these obstacles, we performed mRNA-seq on RNA isolated from small cellular groups by LMD (Fig. 1*A*). We determined the abundance of genes by calculating reads per kilobase of exon model per million mapped reads (RPKM) values for each annotated isoform, and summed all isoform-level RPKMs for each gene (19, 20). RPKM values were highly correlated for all cellular zones, irrespective of sequencing lanes or flow cells (Spearman correlation > 0.92; Fig. 1*C*). Principal component analysis (PCA) indicates that the primary source of variance in our mRNA-seq data are caused by expression differences among transient embryonic zones, with biological or technical replicates for each zone likely contributing little additional variance (Fig. 1*D* and Figs. S1–S3; PCA values in Table S1). These exploratory analyses demonstrate that our LMD–mRNA-seq approach preserves the spatial resolution of gene expression in the developing cortex.

We assessed differential expression after statistical testing of pooled data sets by using a log-linear Poisson model, which has been shown to be highly effective at identifying differentially expressed genes (DEGs) in mRNA-seq data (21, 22). We identified a total of 2,677 DEGs upon imposing a conservative

Author contributions: A.E.A. and P.R. designed research; A.E.A., Y.X., J.C., and M.H.D. performed research; J.P.N. contributed new reagents/analytic tools; A.E.A., S.O., J.L., and J.P.N. analyzed data; and A.E.A., J.P.N., and P.R. wrote the paper.

The authors declare no conflict of interest.

Data deposition: The data reported in this paper have been deposited in the Gene Expression Omnibus (GEO) database, www.ncbi.nlm.nih.gov/geo (accession no. GSE30765).

[1]To whom correspondence should be addressed. E-mail: pasko.rakic@yale.edu.

This article contains supporting information online at www.pnas.org/lookup/suppl/doi:10.1073/pnas.1112213108/-/DCSupplemental.

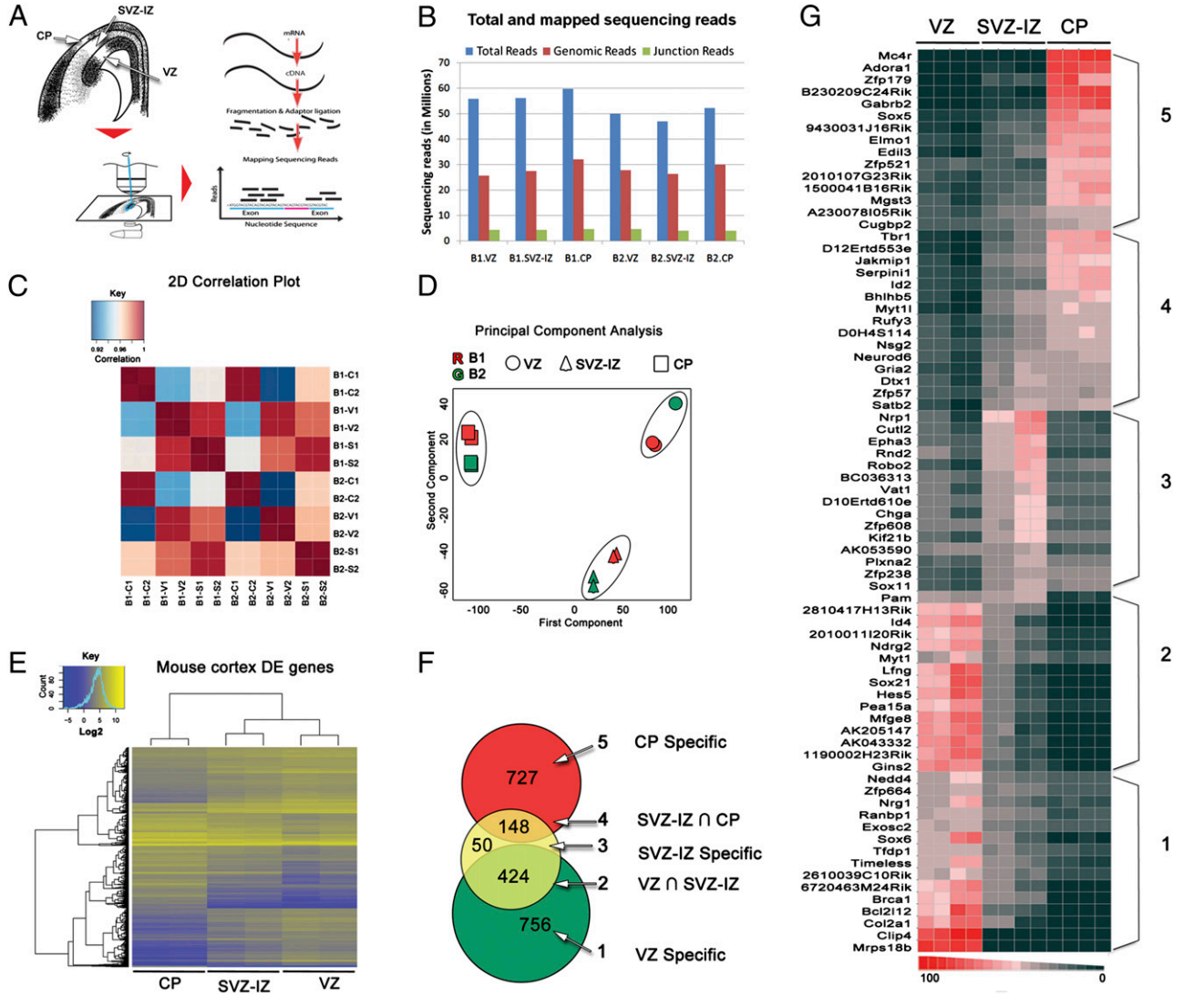

Fig. 1. Determination of zone-specific differential expression. (*A*) Schematic shows experimental steps: we used LMD to isolate each of the cellular zones (VZ, SVZ–IZ, and CP) from E14.5 brains in coronal sections chosen by systematic random sampling. We performed single-end 75-bp RNA sequencing on the Illumina Genome Analyzer IIx. (*B*) Graph shows reads uniquely mapped to the mouse genome and splice junctions compared with the total number of sequencing reads that passed quality checks. (*C*). Two-dimensional correlation plot of gene expression levels between sequencing lanes. Spearman R^2 for each technical replicate and zone are color-coded from 0.92 (blue) to 1 (red). Labels starting with "B1" and "B2" indicate biological replicas 1 and 2 respectively; C, CP; S, SVZ-IZ; V, VZ. (*D*) Principal components analysis plot of $\log_2$-(RPKM) for 12 samples confirms that the correlation of technical replicates is higher than biological replicates, which in turn is much higher than different tissue samples. (*E*). Unsupervised hierarchical clustering of DEGs. RPKM values were $\log_2$-transformed and clustered using the gplots and heatmap.2 packages in R. The color scale (*Top Left*) indicates levels of expression, with yellow corresponding to high expression levels and blue corresponding to low. (*F*) Venn diagram shows zone-specific gene expression after pairwise comparisons. We applied a Benjamini–Hochberg *P* value (bhp < 10^{-5}) and a twofold change in expression to determine DEGs. (*G*). Heat map shows the fractional change in expression for a subset of DEGs in each of the five groups in *B*. Each row represents the fraction of expression from all flow cells for a particular gene (red is highest; black is lowest).

P value ($<10^{-5}$) and a twofold change in expression ($\log_2 > 1$) between at least two cellular zones. We were able to isolate five groups of DEG, three of which were specific to only one zone (groups 1, 3, and 5; Fig. 1*F*). Two additional groups (groups 2 and 4) were differentially expressed in two zones versus the third (VZ ∩ SVZ–IZ and SVZ–IZ ∩ CP), whereas the intersection of VZ- and CP-specific genes did not return any common DEG. Furthermore, we performed unsupervised clustering of all DEGs to identify mRNA specific to each neocortical zone, which supported our differential expression analysis (Fig. 1*E*). The expression patterns across the cortex for a representative set of genes from each group are shown in Fig. 1*G*.

nTARs Are Differentially Distributed Among Embryonic Zones. Transcriptional activity has been reported from regulatory elements located in intergenic regions in cultured E16.5 neurons (23) but not in vivo. Our data contained a significant pool of reads that mapped outside of annotated genes. We defined nTARs based on contiguous coverage and zero overlap with all known genes and 3′UTRs (*Materials and Methods*). After quantification, we analyzed the differential distribution of nTARs using the same statistical methods described later. We found 1,621 differentially expressed nTARs (Table S2) after pairwise comparisons between neocortical zones. We analyzed nTARs for significant overlap with known genomic elements such as enhancers, promoters, and remaining intergenic regions including gene deserts. Only two nTARs overlapped with suspected forebrain enhancers, near *Ngn2* and *Fzd8*, respectively, and one overlapped with a known limb enhancer (24), suggesting that nTARs in our data are less likely transcribed from enhancers. Although 172 nTARs over-

lapped with promoters near zone-specific genes, the majority of nTARs mapped to intergenic areas excluding gene deserts, suggesting the existence of putative unique transcripts showing zone-specific dynamic expression in the mouse neocortex.

Verification of Zone Specific Expression. We chose several zone-specific genes to validate expression levels determined by mRNA-seq. First, we carried out quantitative real time RT-PCR (qRT-PCR) on RNA isolated from each cellular zone by LMD following the same procedures used for mRNA-seq. We performed in situ hybridization (ISH) to map the histological distribution of these genes. The level of gene expression predicted by our analysis of mRNA-seq data were concordant with levels determined by qRT-PCR and tissue distribution determined by ISH (Fig. 2 and Fig. S4). To extend our validation process, we also turned to publicly available resources—the Allen Brain Atlas (ABA) and GenePaint (GP). With the exception of novel genes and transcripts with multiple splice isoforms, all 60 targets we searched for in public databases showed tissue distribution similar to that predicted by our mRNA-seq expression analysis.

Functional Analysis of Zone-Specific Genes. To gain insight into the biological processes and pathways enriched in each transitional zone during corticogenesis, we used each of the five groups of DEGs (Fig. 1*E*) as input to perform Gene Ontology (GO) analysis (Table S3). The most enriched categories in the VZ were related to cell division, which included genes such as cyclins and cyclin-dependent kinases in addition to genes affecting stem-cell renewal such as *Ctnnb1*, *Notch1*, and *Spread1*. Notably, genes involved in transcriptional regulation, such as *Pax6*, *Sox2*, and *Hes1*, were more prominent in group 2 (VZ ∩ SVZ–IZ). The top categories of transcripts enriched in the SVZ–IZ included axonal guidance and cell migration genes such as *Nrp1*, *Plxna2*, and *Dcx*. Genes contributing to axonogenesis and cell migration represented the largest fraction in group 4 (SVZ–IZ ∩ CP), including *Cdlk1*, *Satb2*, and *Cdk5r1*. Analysis of the CP transcriptome showed overrepresentation of functional categories relating to synaptogenesis, exocytosis, and axonogenesis that included genes such as *Cplx1*, *Nav1*, and *Fezf2*. We also investigated overrepresented canonical pathways in addition to GO categories. In the VZ, the most prominent pathways centered on cell cycle regulation, transition through the cell cycle, and termination of the cell cycle. Pathways enriched in the SVZ–IZ included ephrin-dependent axonal guidance, extracellular Ca^{2+}-and nicotine-dependent inhibition of cell cycle progression, as well as regulation of Erk signaling. In the CP, the most prominent pathways were GABA-A receptor trafficking, Reelin/CDK5-mediated neuronal growth, and PKA signaling.

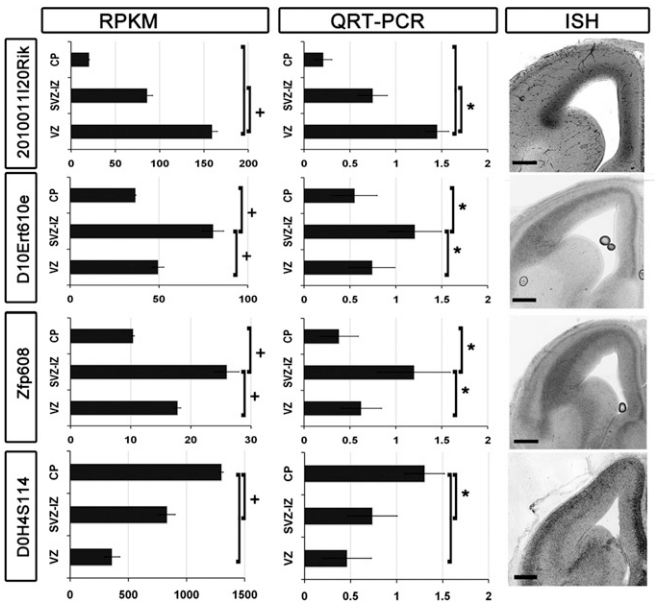

Fig. 2. Verification of zone-specific genes. A row of three panels is shown for every gene named on the left side. The first panel shows mean RPKM expression levels (±SEM). Significance is based on pairwise comparisons and bhp $< 10^{-5}$ (+). The second column of graphs shows qRT-PCR on RNA isolated by LMD from E14.5 cryosections. Mean fold change (±SEM) is plotted for every cellular zone (*$P < 0.001$). The third column shows ISH on E14.5 mouse sections.

Self-Organizing Maps Reveal Functional Insights Into Novel Zone-Specific Genes. Our analysis generated a significant pool of novel, zone-specific genes that were excluded from GO and pathway analyses because of missing annotations. To explore potential relationships between known and novel genes, we used AutoSOME to isolate modules of coexpressed genes (25). First, we performed cluster analysis by comparing expression levels by using the five groups of DEGs (Fig. 1*E*) as input. We then queried the GeneMania (26) database of functional data to identify networks based on self-organizing map (SOM) modules (Table S4). We analyzed stable modules at 45% confidence level and $P \leq 0.05$ (Monte Carlo P value). For example, we examined a module in group 2 (VZ ∩ SVZ–IZ) that contained *Sox2* and *Pax6* (Fig. 3*A*), which have been shown to affect the balance of stem cells and neurogenesis (27). Network analysis shows that *Sox2* and *Pax6* have first-order interactions with *Hes5*, a downstream effector of Notch, and *Sox21*, as well as potential second-order interaction with *Nde1* and *Mfge8* (Fig. 3*A*). We determined potential interactions between the novel SVZ–IZ gene *D10ERT610E* (Fig. 2), and other module members *Nrp1*, *Sema3c*, and *Plxna2* that have been shown to play a role in axonal guidance (Fig. 3*B*). Finally, we assembled a SOM-based network including the novel CP-specific gene *B230209C24RIK* (Fig. 3*C*), which uncovered potential interactions with genes involved in neurotransmitter trafficking and release such as *Cplx1* and *Dync1i1* (Fig. 3*C*). However, the full benefit of gene networks based on SOM modules that contain novel genes can only be achieved with functional studies.

Contribution of Alternative Splicing to Corticogenesis. Although it is presently difficult to gauge the full contribution of alternative splicing to corticogenesis, its importance cannot be dismissed, as studies on *Pax6* and *Tnc* have demonstrated (28, 29). Differential alternative splicing has also been observed in different areas of the normal and diseased human cortex (15, 30). To elucidate how alternative splicing contributes specifically to gene-level expression and globally to corticogenesis, we explored the extent of alternative isoform use by examining isoform-level RPKM values between cortical zones. First, we calculated the relative abundance of transcripts using Cufflinks (20), and then analyzed differentially expressed isoforms (DEIs; Fig. 4*A*) following the same statistical workflow mentioned earlier. Overall, the proportion of DEGs with two or more isoforms was highest in the CP (15.7%) compared with the VZ (11.8%) and the SVZ–IZ (12.8%; Table S2).

We separated zone-specific splice isoforms into six groups based on their differential expression in at least one zone compared with the others (Fig. 4*A*), which highlighted differences between the distribution of DEIs and DEGs. Even though the contribution of splice isoforms to gene-level expression is additive, gene-level expression is confounded by switching events in which an isoform is dominant in one zone but negligible in another. For example, individual splice variants of *Wdr61*, which falls in group 6 (Fig. 4*A*), are differentially expressed (Fig. 4*B*), but *Wdr61* is not differentially expressed at the gene level given our cutoff criteria ($P < 10^{-5}$ and $\log_2 > 1$). Switching of dominant isoforms does not always result in subthreshold differential expression. For instance, of three expressed isoforms for *Mfge8*, which falls in group 2 (VZ ∩ SVZ–IZ) according to our analysis, two are differentially expressed but with different zonal distribution. Isoform 1 of *Mfge8* (UC009hyb.1)

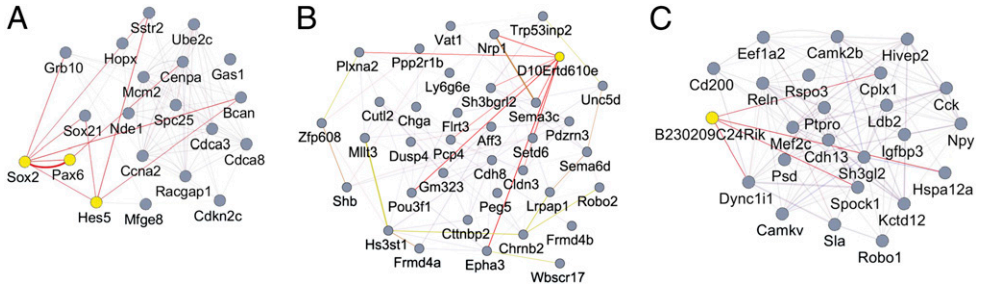

Fig. 3. Network analysis of zone-specific SOM modules. Networks were generated by using the GeneMania large functional association database based on SOM module membership. Edges connecting different nodes (i.e., genes) represent data derived from other studies. (*A*). Representative cluster from VZ ∩ SVZ–IZ highlighting all edges emanating from *Sox2* and *Pax6* to other members of the SOM module. (*B*) Network from SVZ-IZ module highlighting all edges connecting the novel gene *D10Ert610e* to *Nrp1* and *Sema3c*, which are involved in axonogenesis. (*C*). SOM-based network from CP-specific modules shows extensive connections between the novel gene *B230209C24RIK* and *Cplx1* and *Dync1i1*, which are involved in exocytosis.

is highest in the VZ whereas isoform 2 (UC009hya.1) is highly expressed in the VZ and SVZ–IZ versus the CP (Fig. 4*D*). Inspection of *Mfge8*'s histological distribution on ABA and GP revealed VZ-only expression. To investigate this discrepancy, we tested the expression of both isoforms in situ, which confirmed the distribution predicted by our expression analysis. However, for other DEGs with multiple isoforms, such as of *B230209C24RIK*, *Cugbp2*, and *Hes6* (Fig. 4), the expression of splice isoforms changed concomitantly in every zone.

Zone-Specific Transcriptional Regulation. To better understand dynamic developmental events, we sought to identify transcriptional enhancers located near cortex DEGs. Both extreme evolutionary conservation and analysis of the genome-wide binding patterns of the enhancer-associated factor p300, followed by mouse transient transgenic assays, have identified enhancers active in the E11.5 mouse forebrain (24). However, there is little information available about zone-specific enhancers in the cortex or whether enhancers active in E11.5 cortex regulate gene expression at E14.5. With these caveats in mind, we computationally identified candidate zone-specific p300-enriched forebrain enhancers (31) nearest to the transcription start site of DEGs in the E14.5 cortex. We found 181 DEGs with nearby candidate enhancers (Table S5). We also found several verified enhancer elements near DEGs (e.g., *Sox21* and *Tle4*) on the Vista Enhancer Browser. In contrast to alternative promoter use and alternative splicing, enhancer regulation of zone-specific differential expression is a level of genomic regulation that is yet to be empirically explored in the developing neocortex.

Discussion

A fundamental feature of the developing neocortex is that the fate and layer specification of neurons is defined at the time of their birth from neural stem cells in the proliferative VZ and SVZ (1). The transcriptional content of cells as they progress from neural stem cells to differentiated neurons remains to be determined. Although differential expression contributing to the arealization of the neocortex has been described by several groups (14, 15), to date it has not been performed with next-generation sequencing or at the resolution of cellular zones. Here, we provide a comprehensive transcriptome analysis of the birth-to-differentiation axis in vivo with an unprecedented resolution by combining two technologies, mRNA-seq and LMD. The data go beyond a traditional genome-scale screen of genes and splice variants by providing the distribution of nTARs enriched in each embryonic zone and putative *cis*-regulatory elements near DEGs.

In the present study, we collected cells from the neocortex by LMD to better resolve the genetic basis of neuronal birth, migration, and differentiation. As expected, we were able to resolve the transcriptome for each cellular zone at the transcript

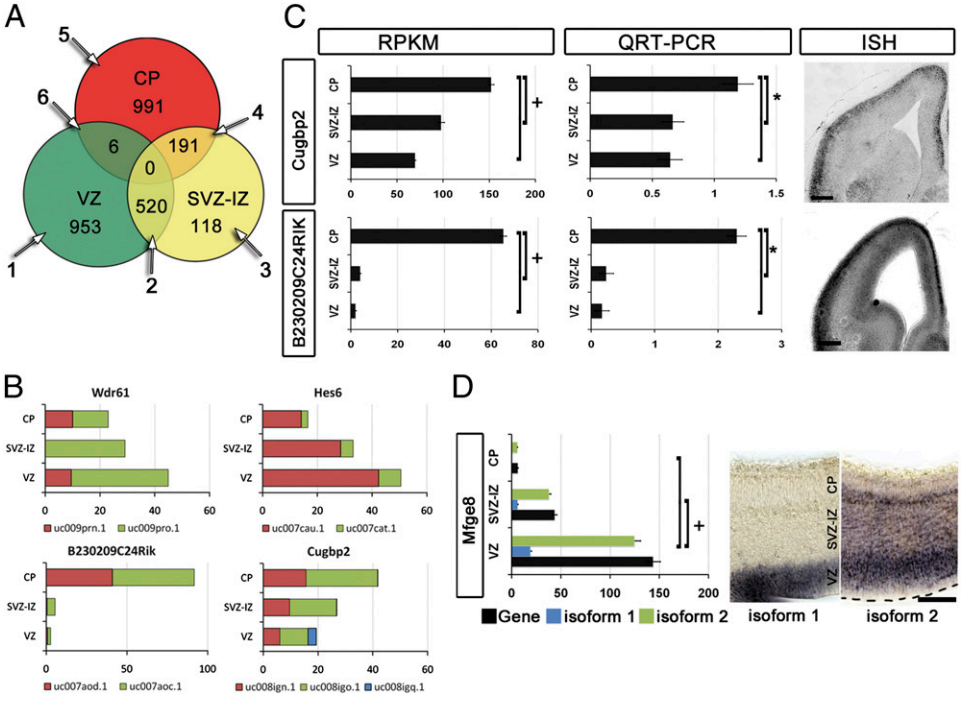

Fig. 4. Distribution and verification of splice isoforms. (*A*). Venn diagram shows the distribution of splice isoforms in six groups after pairwise comparisons, $\log_2$ fold change, and bhp $< 10^{-5}$. (*B*) The expression levels of different isoforms for the same gene are additive. However, isoforms for *Wdr61* have opposing gradients, whereas *Hes6*, *B230209C24Rik*, and *Cugbp2* isoforms have similar expression gradients across zones. (*C*) We verified the expression of *B230209C24Rik* and *Cugbp2* by qRT-PCR after LMD. The first column shows mean RPKM expression levels (±SEM; +, bhp $< 10^{-5}$). The second column of graphs shows mean fold change in qRT-PCR (±SEM) plotted for every cellular zone (*$P < 0.001$). ISH shows that tissue distribution is comparable to the expression gradient determined by the differential analysis. (*D*) *Mfge8* has two DEIs in the neocortex at E14.5 with different expression gradients. The first column shows mean RPKM expression levels (±SEM; +, bhp $<10^{-5}$). We also confirmed the difference in the distribution of isoforms by ISH in the mouse cortex. ISH was performed in parallel by using probes designed to differentiate between the two isoforms.

NEUROSCIENCE

level. As we did not separate cytoarchitectonic regions, we expected our results to be blind to rostrocaudal and mediolateral expression gradients; yet, we were able to detect genes expressed in such gradients (e.g., *Nsg2* and *D0H4S114*; Fig. 2 and Fig. S4). To extend the validation process, we examined the additional DEGs in publicly available databases (GP and ABA), which confirmed the expression gradient predicted with mRNA-seq. However, there was little information available in pubic databases about the histological distribution of novel genes and splice isoforms. Alternative splicing is a major source of protein diversity that affects cellular expression capacity and gene regulation (32). Our data indicate that, in most cases, splice isoforms increase or decrease concomitantly among different embryonic zones (Fig. 4). We also observed switching events whereby the distribution of splice isoforms conflicted with gene level distribution. In these cases, deducing zone-specific distribution of genes is confounded by splice isoform use, alternative transcription-start sites, and complex *cis*-regulation. The data we present here provide a higher level of detail that is necessary, yet currently unavailable, for investigating the combinatorial expression of splice isoforms that may impart slightly different functions during development.

Two major advantages of mRNA-seq versus microarray technology are its ability to provide a digital readout of mRNA levels in cells (17), as well as its high sensitivity in detecting even few copies of mRNA species. The first apparent feature in our data are that more than 65% of detected genes are expressed in all three developmental zones. In our analysis, we found that several mRNAs (e.g., *Sox2* and *Pax6*) expressed by stem cells in the VZ were present in CP neurons days after their birth in the VZ. As the CP is known to be devoid of stem cells at this stage, we speculate that the degradation of mRNA or silencing of gene expression during development proceeds at a much slower pace than the migration of neurons to their destination in the cortex. We also detected the expression of genes involved in neuronal differentiation (33) (e.g., *NeuroD* and *NeuroD2*) at low levels in the VZ, suggesting an anticipatory program that restricts VZ stem cells to a neocortical neuronal fate. These data lends support to the observation that early activation of differentiation genes occurs in VZ progenitors, which was observed in live imaging experiments of the β-III tubulin-driven GFP (34), and that a restrictive program ensues at the onset of neurogenesis in the dorsal telencephalon (35, 36). Alternatively, the detection of differentiation genes may be a result of heterogeneity of cells in the VZ (37, 38).

Indeed, the VZ at midcorticogenesis contains a heterogeneous population of cells, including radial glia, INPs, and short neuronal progenitors (38, 39) that generate upper layer neurons (4, 33, 40). The predominant function deduced from the VZ transcriptome is cell cycle regulation, which reflects the density and principal role of neural stem cells in the VZ (Table S3). Our functional enrichment analysis also supports a great body of work assigning fate determination and diversification of neuronal types to progenitors in the VZ (1, 41). Furthermore, our analysis identified several pathways enriched in the VZ and SVZ–IZ that seem to be disrupted in cancerous cells. Indeed, a big proportion of infantile supratentorial malignancies originate from stem cells that reside in the VZ and SVZ–IZ (42). As the mouse remains the most used animal model for normal and pathological development, data presented here raise the possibility of finding new tumor-promoting regulatory cascades, and therefore novel therapeutic agents.

The SVZ–IZ region is the major throughway in the developing neocortex, as it contains PNs and INPs (1). PNs initiate the formation of axons soon after entering this zone (5, 43), and engage in complex navigational maneuvering to find their ultimate destination (44). INPs amplify the number of neurons generated in the VZ (6, 45) and are thought to be responsible for the evolutionary expansion in cortical thickness (46, 47), but whether they contribute to increased diversification in cortical layers or solely to increasing neuronal numbers is not known. Our data indicate that genes involved in cell cycle regulation are enriched in both the VZ and SVZ–IZ. This suggests that the total size of the neuronal population depends on the mitotic activity in both zones. Fate-determination genes were enriched in both zones, albeit more so in group 2 (VZ ∩ SVZ–IZ), indicating that INPs in the SVZ–IZ may also contribute to fate specification. Our results support the currently accepted theory that fate specification occurs at the time of birth in the VZ (1) but raises the possibility that further specification ensues in the SVZ–IZ. Determining the function of SVZ–IZ–specific novel transcription factors (e.g., *Zfp608*, *Myt1*, and *Zfp238*) may explain whether they contribute to an independent specification program or an intermediary implementation of the protomap. In the mouse cortex, a small population of $Sox2^+$ cells are scattered in the SVZ–IZ, but only the most lateral region of the SVZ–IZ contains a sizable pool of $Pax6^+$ cells. However, it is not known if these $Sox2^+$/$Pax6^+$ cells perform the same function as stem cells that reside in the much-expanded SVZ of the human embryonic brain (46, 47).

The CP at this stage of development is composed of pyramidal neurons that project to subcortical areas including the spinal cord, pons, and midbrain. These neurons grow elaborate dendritic trees to receive proper input. Recent evidence suggests that final differentiation mechanisms do not occur until neurons settle in the CP (48, 49). Indeed, our transcriptome analysis exposed CP-enriched genes and splice isoforms involved in the maturation programs, including dendritic growth, synaptogenesis, exocytosis, and axonogenesis. Furthermore, our analysis uncovered genes associated with tumorigenesis (*Sox11*) (50), mental retardation (*Kirrel3*) (51), and schizophrenia (*Gabrb2*) (52), but their contribution to normal differentiation and signaling processes in the cortex is not yet understood.

Through high-resolution transcriptome analysis, we define five transcriptional programs that contain genes necessary for stem cell maintenance, neurogenesis, migration, and differentiation (Fig. 1*F*). We expect our functional analyses to facilitate in vivo testing of gene network relationships and candidate *cis*-regulatory sequences. Finally, our high-resolution transcriptome map of the mouse transient zones opens the door for determining evolutionary conserved processes, as well as species-specific differences, with embryonic human transient cellular zones.

Materials and Methods

Hi-Resolution mRNA-seq. Cells were collected from fresh frozen tissue by LMD. Sequencing libraries were prepared after RNA extraction and then sequenced using the Illumina GA IIx.

Further experimental details can be found in *SI Materials and Methods*.

ACKNOWLEDGMENTS. The authors acknowledge the technical assistance of Mariamma Pappy, as well as Paul Zumbo and Shrikant Mane at the Yale Center for Genome Analysis. We also thank members of the Rakic and Noonan laboratories for critical comments on the manuscript. This work was supported by National Institutes of Health (NIH) Grants DA02399 (to P.R.) and GM094780 (to J.P.N.), the Patterson Trust Fellowship in Brain Circuitry (A.E.A), and the Kavli Institute for Neuroscience at Yale University. The Yale University Biomedical High Performance Computing Center is supported by NIH Grant RR19895.

1. Rakic P, Ayoub AE, Breunig JJ, Dominguez MH (2009) Decision by division: Making cortical maps. *Trends Neurosci* 32:291–301.
2. Bystron I, Blakemore C, Rakic P (2008) Development of the human cerebral cortex: Boulder Committee revisited. *Nat Rev Neurosci* 9:110–122.
3. Rakic P (1988) Specification of cerebral cortical areas. *Science* 241:170–176.
4. Takahashi T, Goto T, Miyama S, Nowakowski RS, Caviness VS, Jr. (1999) Sequence of neuron origin and neocortical laminar fate: relation to cell cycle of origin in the developing murine cerebral wall. *J Neurosci* 19:10357–10371.
5. Noctor SC, Martínez-Cerdeño V, Ivic L, Kriegstein AR (2004) Cortical neurons arise in symmetric and asymmetric division zones and migrate through specific phases. *Nat Neurosci* 7:136–144.
6. Kowalczyk T, et al. (2009) Intermediate neuronal progenitors (basal progenitors) produce pyramidal-projection neurons for all layers of cerebral cortex. *Cereb Cortex* 19:2439–2450.
7. Gaitanis JN, Walsh CA (2004) Genetics of disorders of cortical development. *Neuroimaging Clin N Am* 14:219–229.

8. Gohlke JM, et al. (2008) Characterization of the proneural gene regulatory network during mouse telencephalon development. *BMC Biol* 6:15.
9. Sansom SN, et al. (2009) The level of the transcription factor Pax6 is essential for controlling the balance between neural stem cell self-renewal and neurogenesis. *PLoS Genet* 5:e1000511.
10. Rakic P (2006) A century of progress in corticoneurogenesis: From silver impregnation to genetic engineering. *Cereb Cortex* 16(suppl 1):i3–i17.
11. Ajioka I, Nakajima K (2005) Birth-date-dependent segregation of the mouse cerebral cortical neurons in reaggregation cultures. *Eur J Neurosci* 22:331–342.
12. Chen JG, Rasin MR, Kwan KY, Sestan N (2005) Zfp312 is required for subcortical axonal projections and dendritic morphology of deep-layer pyramidal neurons of the cerebral cortex. *Proc Natl Acad Sci USA* 102:17792–17797.
13. Tachikawa K, Sasaki S, Maeda T, Nakajima K (2008) Identification of molecules preferentially expressed beneath the marginal zone in the developing cerebral cortex. *Neurosci Res* 60:135–146.
14. Kudo LC, Karsten SL, Chen J, Levitt P, Geschwind DH (2007) Genetic analysis of anterior posterior expression gradients in the developing mammalian forebrain. *Cereb Cortex* 17:2108–2122.
15. Johnson MB, et al. (2009) Functional and evolutionary insights into human brain development through global transcriptome analysis. *Neuron* 62:494–509.
16. Winden KD, et al. (2009) The organization of the transcriptional network in specific neuronal classes. *Mol Syst Biol* 5:291.
17. Wang Z, Gerstein M, Snyder M (2009) RNA-Seq: A revolutionary tool for transcriptomics. *Nat Rev Genet* 10:57–63.
18. Han X, et al. (2009) Transcriptome of embryonic and neonatal mouse cortex by high-throughput RNA sequencing. *Proc Natl Acad Sci USA* 106:12741–12746.
19. Langmead B, Trapnell C, Pop M, Salzberg SL (2009) Ultrafast and memory-efficient alignment of short DNA sequences to the human genome. *Genome Biol* 10:R25.
20. Trapnell C, et al. (2010) Transcript assembly and quantification by RNA-Seq reveals unannotated transcripts and isoform switching during cell differentiation. *Nat Biotechnol* 28:511–515.
21. Marioni JC, Mason CE, Mane SM, Stephens M, Gilad Y (2008) RNA-seq: An assessment of technical reproducibility and comparison with gene expression arrays. *Genome Res* 18:1509–1517.
22. Bullard JH, Purdom E, Hansen KD, Dudoit S (2010) Evaluation of statistical methods for normalization and differential expression in mRNA-Seq experiments. *BMC Bioinformatics* 11:94.
23. Kim TK, et al. (2010) Widespread transcription at neuronal activity-regulated enhancers. *Nature* 465:182–187.
24. Visel A, et al. (2009) ChIP-seq accurately predicts tissue-specific activity of enhancers. *Nature* 457:854–858.
25. Newman AM, Cooper JB (2010) AutoSOME: A clustering method for identifying gene expression modules without prior knowledge of cluster number. *BMC Bioinformatics* 11:117.
26. Warde-Farley D, et al. (2010) The GeneMANIA prediction server: Biological network integration for gene prioritization and predicting gene function. *Nucleic Acids Res* 38 (web server issue):W214–W220.
27. Guillemot F (2007) Cell fate specification in the mammalian telencephalon. *Prog Neurobiol* 83:37–52.
28. von Holst A, Egbers U, Prochiantz A, Faissner A (2007) Neural stem/progenitor cells express 20 tenascin C isoforms that are differentially regulated by Pax6. *J Biol Chem* 282:9172–9181.
29. Berger J, et al. (2007) Conditional activation of Pax6 in the developing cortex of transgenic mice causes progenitor apoptosis. *Development* 134:1311–1322.
30. Twine NA, Janitz K, Wilkins MR, Janitz M (2011) Whole transcriptome sequencing reveals gene expression and splicing differences in brain regions affected by Alzheimer's disease. *PLoS ONE* 6:e16266.
31. Blow MJ, et al. (2010) ChIP-Seq identification of weakly conserved heart enhancers. *Nat Genet* 42:806–810.
32. Black DL (2000) Protein diversity from alternative splicing: A challenge for bioinformatics and post-genome biology. *Cell* 103:367–370.
33. Mattar P, et al. (2008) Basic helix-loop-helix transcription factors cooperate to specify a cortical projection neuron identity. *Mol Cell Biol* 28:1456–1469.
34. Attardo A, Calegari F, Haubensak W, Wilsch-Bräuninger M, Huttner WB (2008) Live imaging at the onset of cortical neurogenesis reveals differential appearance of the neuronal phenotype in apical versus basal progenitor progeny. *PLoS ONE* 3:e2388.
35. McCarthy M, Turnbull DH, Walsh CA, Fishell G (2001) Telencephalic neural progenitors appear to be restricted to regional and glial fates before the onset of neurogenesis. *J Neurosci* 21:6772–6781.
36. Shen Q, et al. (2006) The timing of cortical neurogenesis is encoded within lineages of individual progenitor cells. *Nat Neurosci* 9:743–751.
37. Gal JS, et al. (2006) Molecular and morphological heterogeneity of neural precursors in the mouse neocortical proliferative zones. *J Neurosci* 26:1045–1056.
38. Stancik EK, Navarro-Quiroga I, Sellke R, Haydar TF (2010) Heterogeneity in ventricular zone neural precursors contributes to neuronal fate diversity in the postnatal neocortex. *J Neurosci* 30:7028–7036.
39. Soriano E, Dumesnil N, Auladell C, Cohen-Tannoudji M, Sotelo C (1995) Molecular heterogeneity of progenitors and radial migration in the developing cerebral cortex revealed by transgene expression. *Proc Natl Acad Sci USA* 92:11676–11680.
40. Nieto M, et al. (2004) Expression of Cux-1 and Cux-2 in the subventricular zone and upper layers II-IV of the cerebral cortex. *J Comp Neurol* 479:168–180.
41. Desai AR, McConnell SK (2000) Progressive restriction in fate potential by neural progenitors during cerebral cortical development. *Development* 127:2863–2872.
42. Grondin RT, Scott RM, Smith ER (2009) Pediatric brain tumors. *Adv Pediatr* 56: 249–269.
43. Hatanaka Y, et al. (2009) Distinct roles of neuropilin 1 signaling for radial and tangential extension of callosal axons. *J Comp Neurol* 514:215–225.
44. Torii M, Hashimoto-Torii K, Levitt P, Rakic P (2009) Integration of neuronal clones in the radial cortical columns by EphA and ephrin-A signalling. *Nature* 461:524–528.
45. Sessa A, Mao CA, Hadjantonakis AK, Klein WH, Broccoli V (2008) Tbr2 directs conversion of radial glia into basal precursors and guides neuronal amplification by indirect neurogenesis in the developing neocortex. *Neuron* 60:56–69.
46. Hansen DV, Lui JH, Parker PR, Kriegstein AR (2010) Neurogenic radial glia in the outer subventricular zone of human neocortex. *Nature* 464:554–561.
47. Fietz SA, et al. (2010) OSVZ progenitors of human and ferret neocortex are epithelial-like and expand by integrin signaling. *Nat Neurosci* 13:690–699.
48. Joshi PS, et al. (2008) Bhlhb5 regulates the postmitotic acquisition of area identities in layers II-V of the developing neocortex. *Neuron* 60:258–272.
49. Kwan KY, et al. (2008) SOX5 postmitotically regulates migration, postmigratory differentiation, and projections of subplate and deep-layer neocortical neurons. *Proc Natl Acad Sci USA* 105:16021–16026.
50. Stuart JE, et al. (2010) Identification of gene markers associated with aggressive meningioma by filtering across multiple sets of gene expression arrays. *J Neuropathol Exp Neurol* 70:1–12.
51. Bhalla K, et al. (2008) Alterations in CDH15 and KIRREL3 in patients with mild to severe intellectual disability. *Am J Hum Genet* 83:703–713.
52. Pun FW, et al. (2010) Imprinting in the schizophrenia candidate gene GABRB2 encoding GABA(A) receptor beta(2) subunit. *Mol Psychiatry* 16:557–568.

Cerebral Cortex November 2007;17:2585–2592
doi:10.1093/cercor/bhl164
Advance Access publication January 27, 2007

Nestin-CreER Mice Reveal DNA Synthesis by Nonapoptotic Neurons following Cerebral Ischemia–Hypoxia

Kevin A. Burns[1], Albert E. Ayoub[2], Joshua J. Breunig[2], Faisal Adhami[1,3], Wei-Lan Weng[1], Melissa C. Colbert[4], Pasko Rakic[2] and Chia-Yi Kuan[1]

[1]Divisions of Developmental Biology and Pediatric Neurology, Cincinnati Children's Hospital Medical Center, University of Cincinnati College of Medicine, 3333 Burnet Avenue, Cincinnati, OH 45229, USA, [2]Department of Neurobiology, Yale University School of Medicine, Kavli Institute for Neuroscience at Yale, New Haven, CT 06510, USA, [3]Physician Scientist Training Program and [4]Division of Molecular Cardiovascular Biology, Cincinnati Children's Hospital Medical Center, University of Cincinnati College of Medicine, 3333 Burnet Avenue, Cincinnati, OH 45229, USA

The standard method of detecting neurogenesis uses bromodeoxyuridine (BrdU) to label DNA synthesis followed by double labeling with neuronal markers. However, DNA synthesis may occur in events unrelated to neurogenesis including aneuploidy and abortive cell cycle reentry. Hence, it is important to confirm neurogenesis with methods other than BrdU incorporation. To this end, we have generated transgenic nestin-CreER mice that express tamoxifen-inducible Cre recombinase under the control of a nestin enhancer. When crossed with a ubiquitous Enhanced Green Fluorescent Protein (EGFP)-Cre-reporter line, the bitransgenic animals can reveal the nestin-positive progenitors and their progeny with EGFP after tamoxifen induction. This system has many applications including visualization of embryonic neural progenitors, detection of postnatally transformed radial glial cells, and labeling adult neural progenitors in the subventricular zone (SVZ). To examine the contribution of SVZ progenitors to cell replacement after stroke, tamoxifen-induced mice were challenged with focal ischemia or combined ischemia–hypoxia followed by BrdU injection. This analysis revealed only very few EGFP-positive cells outside the SVZ after focal ischemia but robust DNA synthesis by hippocampal neurons without immediate cell death following ischemia–hypoxia. These results suggest that the nestin-CreER system is a useful tool for detecting embryonic and adult neurogensis. They also confirm the existence of nonproliferative DNA synthesis by old neurons after experimental brain injury.

Keywords: BrdU, ischemia–hypoxia, lineage tracing, MCAO, neural stem cells, tamoxifen

Introduction

Adult neurogenesis is often studied using bromodeoxyuridine (BrdU) or other thymidine analogues to label DNA synthesis in nascent neurons during the S-phase of the cell cycle. Although BrdU immunocytochemistry is a powerful method, it has shortcomings that may complicate the study of adult neurogenesis after brain injury (Nowakowski and Hayes 2000; Rakic 2002; Kempermann 2005). For example, BrdU incorporation merely indicates DNA synthesis, which may occur in old neurons after cell cycle reentry or in events leading to aneuploidy (Rehen et al. 2001; Herrup et al. 2004). Furthermore, the existence of viable polyploid neurons in normal brains suggests that nonproliferative DNA synthesis may not lead to immediate cell death (Kingsbury et al. 2005). We have recently shown that the combination of cerebral ischemia and hypoxia stimulates DNA synthesis in damaged neurons (Kuan et al. 2004). Hence, in studies of disease and injury, it is particularly important to verify de novo neurogenesis using methods other than BrdU incorporation.

Due to these limitations of BrdU immunocytochemistry, several genetic methods have recently been developed for detecting neurogenesis. An established method is to infect neural progenitors with replication-deficient retrovirus carrying a lineage marker such as the green fluorescence protein (GFP) (Noctor et al. 2001; van Praag et al. 2002). However, this method requires precise injection of the virus into embryos or animals, which can become technically demanding or label only a small number of progenitors. Another useful tool is the transgenic nestin-GFP mice, which express GFP under the control of the nestin promoter or enhancer sequence (Yamaguchi et al. 2000; Kawaguchi et al. 2001; Mignone et al. 2004). Although nestin-GFP mice allow visualization of neural progenitors, they have limited use for lineage tracing because the descendants no longer express GFP after the progenitor-specific nestin gene is downregulated. Recently, a transgenic tetracycline-inducible Cre system was introduced to label nestin-positive progenitors and their progeny (Yu et al. 2005). However, this system is complicated by the requirement of 3 separate transgenes (tTA, TetOp-Cre, and the Cre-reporter gene) to detect the descendants of nestin-positive progenitors.

Recently, the tamoxifen-inducible Cre/loxP recombination system has shown promise as a new strategy to label specific progenitors and their descendants. In this system, transgenic mice are generated using a cell type–specific promoter to express Cre recombinase fused with a tamoxifen-specific binding domain of mutated estrogen receptor (Cre-ERT1 or Cre-ERT2) (Imai et al. 2001; Hayashi and McMahon 2002). When crossed with a ubiquitous Cre-reporter line, the resulting bitransgenic animals allow for temporally controlled lineage tracing after tamoxifen induction. This system has been used to detect adult neural progenitors that respond to Sonic hedgehog signaling in Gli1-CreER mice (Ahn and Joyner 2005), as well as the progeny of neural progenitors using the nestin promoter and enhancer sequences in nestin-CreERT2 mice (Carlen et al. 2006; Imayoshi et al. 2006). We have independently generated nestin-CreER(T1) mice. Here we report that the nestin-CreER system can be used in different ways for studying neurogenesis. We have also used this method in conjunction with BrdU immunocytochemistry to demonstrate the existence of DNA synthesis by nonapoptotic neurons in the hippocampus following ischemia–hypoxia brain injury.

Materials and Methods

Generation of Transgenic Mice

A 1.5-kb polymerase chain reaction (PCR) product containing the nestin second intron enhancer/hsp68 minimal promoter (a gift of Dr S.

Goldman) was subcloned into the pcDNA3 vector using the *Bgl*II/*Hin*dIII sites, thus replacing the cytomegalovirus promoter. A 1.6-kb PCR product encoding Cre recombinase fused to the mutant estrogen receptor (a gift of Dr A. McMahon) was cloned into the nestin/pcDNA3 construct using the *Not*1/*Apa*1 sites. The nestin/hsp68-CreER construct was released from its backbone using *Hin*cII and then injected into the pronuclei of fertilized C57BL/6 eggs by the in-house transgenic mouse facility. Founders were detected by both PCR and Southern blot analysis using a 500-bp probe within the region encoding Cre recombinase. Three separate lines were established with similar Cre activity patterns. The generation of EGFP-Cre-reporter mice (CAG-CAT-EGFP) has been described elsewhere (Nakamura et al. 2006).

Tamoxifen Treatment and Histology

To induce Cre activity in bitransgenic (nestin-CreER and CAG-CAT-EGFP) mice, pregnant dams were induced with a single dose of tamoxifen (Sigma, St Louis, MO) dissolved in corn oil (5 mg per 40 g body weight) on the indicated embryonic days, and adult animals were injected once daily for 4 days with 4 mg per 30 g body weight of tamoxifen dissolved in corn oil. Adult animals were sacrificed by overdose of Avertin, followed by transcardiac perfusion of 4% paraformaldehyde. Brains were postfixed overnight in 4% paraformaldehyde, cryoprotected using 30% sucrose, embedded in Tissue-Tek Optimal Cutting Temperature Compound (Sakura Finetek USA, Torrence, CA), and flash frozen using 2-methyl-butane chilled with dry ice. Frozen brains were sectioned using a cryostat at either 16 μm thickness for mounting on slides or 50 μm for free-floating staining. Standard histological techniques were employed using the following antibodies: EGFP (Molecular Probes, 1:1500), nestin (Chemicon, Temecula, CA, 1:1000), Glutamate Aspartate Transporter (GLAST) (Chemicon, Temecula, CA, 1:4000), glial fibrillary acidic protein (GFAP) (Dako, Glostrup, Denmark, 1:1000), tyrosine hydroxylase (Chemicon, Temecula, CA, 1:1000), doublecortin (DCX) (Chemicon, Temecula, CA, 1:4000), NeuN (Chemicon, Temecula, CA, 1:1000). Secondary/tertiary antibodies used included biotinylated anti-mouse, anti-rabbit, and anti-guinea pig (Vector Labs, Burlingame, CA 1:400); AlexaFluor488-conjugated anti-rabbit (Molecular Probes, Eugene, OR 1:1500); and AlexaFluor594-conjugated streptavidin (Molecular Probes, Eugene, OR 1:1000). Terminal deoxynucleotidyl transferase–mediated dUTP nick end labeling (TUNEL) stain was performed as previously described (Kuan et al. 2004). For double labeling with BrdU, the second epitope was stained for, as usual, to completion. This was followed by acid treatment (2 N HCl and 0.5% Triton-X100 diluted in phosphate-buffered saline [PBS]) for at least 1 h to denature DNA/expose BrdU epitope, washed with PBS, and stained by standard protocol thereafter using rat anti-BrdU (Serotech 1:100) followed by biotinylated anti-rat (Vector Labs, Burlingame, CA 1:400), and AlexaFluor594-conjugated streptavidin. All tissues prepared for fluorescence microscopy were counterstained with 4′,6-diamidino-2-phenylindole (Molecular Probes, Eugene, OR) and mounted using Vectashield (Vector Labs, Burlingame, CA) to preserve fluorescence. Samples were visualized using either an Olympus epifluorescent microscope (BX-51) or a Zeiss confocal microscope (LSM 510).

Organotypic Slice Cultures

Slice cultures were performed as previously described with minor modifications (Gal et al. 2006). Briefly, EGFP-positive embryos were removed from the uterus on E12.5 by a C-section and quickly immersed in ice-cold artificial cerebrospinal fluid (126.0 mM NaCl, 3.0 mM KCl, 1.3 mM $MgSO_4$, 2.5 mM $CaCl_2$, 1.2 mM NaH_2PO_4, 26 mM $NaHCO_3$, and 20 mM dextrose). Brains were supported with 3% low melting agar and sliced at 250 μm thickness on a vibraslicer (WPI, Sarasota, FL). Subsequently, slices were gently separated and moved to collagen-coated culture inserts (Millipore, Bedford, MA) over 1 ml Neurobasal media (GIBCO, Grand Island, NY; supplemented with 5% B27 and 1% N2 supplements, 1% Glutamax, 10% 4-(2-hydroxyethyl)-1-piperazineethanesulfornic acid, and 0.5% penicillin/streptomycin) and incubated at 37 °C and 5% CO_2 atmosphere.

Multiphoton Live Imaging

Imaging was performed on a LSM 510 Meta confocal scanning microscope (Carl Zeiss Inc., Thornwood, NY) coupled to a Mira 900F pumped with 8.0 W Verdi laser (Coherent Inc., Santa Clara, CA) tuned to 890 nm to excite EGFP. After a 2-h recovery period in the incubator, slices were moved to a RC25 recording chamber (Warner Instruments, Hamden, CT), maintained at 36.5 °C, and constantly perfused with culture media (same as above). We focused our data collection on dividing cells in the ventricular zone (VZ) and subventricular zones (SVZs) and migrating cells in the intermediate zone. *Z* stacks (20 × 2 μm) were collected every 10 min from within the slice through a 63× water-immersed objective. Time series were imported into the Axiovision software (Carl Zeiss) for 3-dimensional deconvolution and 4-dimensional reconstruction.

Animal Model of Stroke

The cerebral ischemia–hypoxia model was performed as described (Adhami et al. 2006). The middle cerebral artery occlusion (MCAO) model was performed as described (Longa et al. 1989).

Results

Generation of Nestin–CreER Mice

We generated 3 lines of nestin–CreER mice using the rat nestin second intron enhancer fused to a minimal hsp68 promoter (E/nestin-hsp68 promoter, see Kawaguchi et al. 2001) to express a tamoxifen-inducible Cre recombinase. The nestin-CreER mice were then crossed to a line of Cre-dependent EGFP-reporter mice (Nakamura et al. 2006) to derive bitransgenic nestin-CreER/EGFP-Cre-reporter mice (hereafter referred to as bitransgenic mice). In bitransgenic mice, the E/nestin-hsp68 promoter directs the expression of CreER protein in nestin-positive progenitors (step 1 in Fig. 1*A*). In the absence of tamoxifen, the CreER protein remains in an inactive state outside the nucleus. After tamoxifen induction, the active metabolite 4-hydroxytamoxifen allows CreER to enter the nucleus (step 2) and excise the CAT gene allowing EGFP expression driven by the ubiquitous CMV-β-actin promoter (step 3). Thus, in contrast to nestin-GFP mice, the nestin-CreER system converts nestin expression in precursors into permanent lineage tracing of their descendant cells after tamoxifen induction (Fig. 1*B*).

Imaging Early Neural Progenitor Proliferation

In bitransgenic embryos dosed with tamoxifen at E16.5 (4 mg to the mother) and sacrificed on E18.5, many EGFP-expressing cells were detected in the telencephalic VZ and SVZ (Fig. 1*C*). Some EGFP-positive cells in the VZ have long nestin-positive processes, indicating that they belong to the radial glia subpopulation of neural progenitors (radial glial cells [RGC], arrows in Fig. 1*C,D*) (Noctor et al. 2001). However, there are many more non-RGC EGFP-expressing cells in the VZ and SVZ (asterisk in Fig. 1*C,D*). To test whether these EGFP-expressing cells are also progenitors, we employed real-time confocal imaging of brain slices to look for cell division. In this experiment, bitransgenic embryos dosed with tamoxifen (2 mg) on E10.5 and E11.5 were sacrificed on E12.5, and their brains were harvested for telencephalic slice cultures. This real-time analysis showed cell division and interkinetic nuclear oscillation of EGFP-positive progenitors in the VZ (data not shown). In addition, proliferation of EGFP-positive cells in the SVZ of E12.5 cortex can be visualized with a high signal-to-noise ratio (Fig. 1*E,F*; see Supplementary Video). Together, these results suggest the nestin-CreER system labels embryonic neural progenitors.

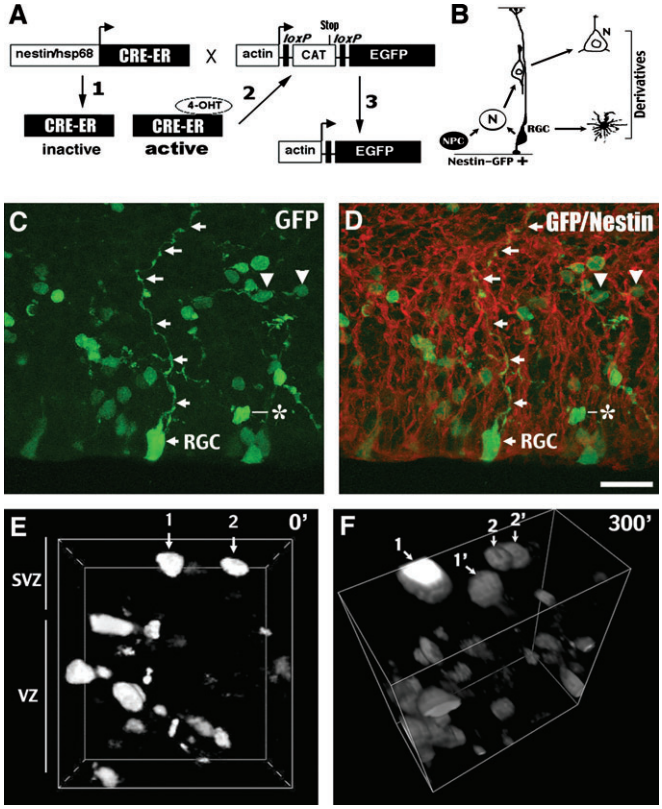

Figure 1. The nestin-CreER system labels neural progenitors and radial glial cells. (*A*) Schematic diagram of the nestin-CreER and EGFP-Cre-reporter system for labeling nestin-positive progenitors and their progeny. nestin/hsp68: the nestin second intron enhancer fused to a hsp68 minimal promoter. Cre-ER: Cre recombinase fused with the tamoxifen-inducible estrogen receptor. 4-OHT: 4-hydroxytamoxifen. The EGFP-Cre-reporter line uses a ubiquitous β-actin promoter fused with the CMV enhancer element. (*B*) Only neural progenitor cells (NPC) and RGC are labeled in nestin-GFP mice, whereas nestin-CreER system also detects the derivatives of NPC and RGC. (*C, D*) In E18.5 bitransgenic (nestin-CreER/EGFP-reporter) embryos induced with tamoxifen on E16.5, cells expressing EGFP include nestin-positive RGC with a long radial fiber (arrows), tangentially migrating neurons (arrowheads), and non-RGC neural progenitors (asterisk). (*E, F*) Time-lapse imaging shows the division of 2 non-RGC neural progenitors (arrows) in the SVZ in E12.5 embryos over a period of 5 h. The projection of the *z* axis stacked images in (*F*) is rotated 35° to confirm the division and separation of the daughter cells. (See also Supplemental Video 1). Scale bar: 20 μm in (*C, D*).

Tracing the Derivatives of Embryonic Nestin-Positive Progenitors

The nestin-CreER system can also label the progeny of nestin-positive progenitors. For example, in E17.5 bitransgenic embryos dosed with tamoxifen at E14.5, there are many EGFP-positive migrating neurons in the cortical plate (arrowheads in Fig. 2*A–C*) in addition to EGFP/GLAST double-positive RGCs in the SVZ (arrows in Fig. 2*A–C*). To test the temporal control of lineage tracing in this system, we injected one dose of tamoxifen to pregnant mice at E14 or E18 (the former is during the period of cortical neurogenesis, whereas the latter is after cortical neurogenesis) and compared the cell types of EGFP-positive cells in the postnatal brain. We found that E14-tamoxifen induction labeled many cortical neurons (type 1 in Fig. 2*D,F*; colabeled for NeuN, see Supplementary Fig. 1) that were located in and above layer IV of the cerebrum consistent with the inside-out sequence of cortical neurogenesis. Furthermore, the type 1 cells (cortical neurons) were not labeled by E19-tamoxifen induction (Fig. 2*E*), further confirming their neuronal identity. EGFP-labeled interneurons derived from the ganglionic eminences were also observed throughout the entire cortex (data not shown). Interestingly, E19-tamoxifen injection detects a population of large, highly branched EGFP-positive cells (type 2 in Fig. 2*D,E*), without labeling cortical neurons. These type 2 cells were distributed in all layers of the cortex and express the astrocyte marker GFAP in the proximal branches (Fig. 2*G–I*), suggesting that they are astrocytically transformed RGC (Schmechel and Rakic 1979; Voigt 1989). Using the nestin-CreER system, we can also label cerebellar Purkinje cells, granule cells, or Bergmann glia depending on the timing of tamoxifen induction (data not shown). Together, these results suggest the nestin-CreER system offers temporally regulated lineage tracing to label some specific populations of cells in the nervous system.

Detecting Adult Neurogenesis by Progenitors in the SVZ

The nestin-CreER system can be used to detect adult neurogenesis by initiating tamoxifen induction after birth. To test this application, we injected 4 doses of tamoxifen (4 mg) to 5-week-old bitransgenic mice and sacrificed them 10 days later to detect EGFP-expressing cells. We found many EGFP-positive cells in the SVZ near the lateral ventricles (Fig. 3*A*), some of which also express GFAP (Fig. 3*B,C*, see also Supplementary Fig. 2). This result suggests the nestin-Cre-ER system can label the astrocyte-like SVZ precursors (B cells) and their descendants in the adult brain (Doetsch et al. 1999). Consistent with this notion, we detected many EGFP-positive cells expressing the migratory neuroblast marker DCX in the rostral migratory stream (RMS) of tamoxifen-dosed bitransgenic mice (Fig. 3*D–F*). In addition, many EGFP-expressing cells were found exiting the RMS to migrate toward the glomerular regions in the olfactory bulb (Fig. 3*J,K*). The EGFP-positive cells in the periglomerular region express interneuron markers including tyrosine hydroxylase (Fig. 3*J–L*).

We found that the expression of EGFP requires tamoxifen induction in both male and female bitransgenic mice (Fig. 3*L*, $n > 10$), indicating the stringency of the inducible CreER(T1) activity. However, there are limitations of the nestin-CreER system. In all 3 lines of nestin-CreER mice, the dentate gyrus subgranular zone (SGZ) progenitors were not labeled, in contrast to the consistent labeling of SVZ progenitors in every tamoxifen-induced bitransgenic animal. Some EGFP-positive cells were occasionally found in the normally nonneurogenic regions after tamoxifen induction, including the SVZ of the third ventricle, the hippocampal pyramidal cell layer, and the cingulate cortex (Supplementary Fig. 3). The cause of this "false-negative" and "false-positive" labeling may be due to the E/nestin-hsp68 promoter in the transgenic mice (see Discussion).

Minimal SVZ-Derived Neurogenesis and Ectopic Migration following Focal Ischemia

Previous studies have indicated that cell replacement after stroke primarily comes from the SVZ progenitors, rather than the dentate gyrus SGZ progenitors (Arvidsson et al. 2002). Thus, although the nestin-CreER system does not label SGZ progenitors, it can still be used for detecting the SVZ-derived neurogenesis and potential cell replacement following stroke. For this study, bitransgenic mice were given 4 doses of tamoxifen over 4 days and then rested for 14 days to allow the clearance of tamoxifen prior to the stroke challenge. After stroke, the tamoxifen-dosed mice were injected with 4 doses of BrdU (100 mg/kg) over 2 days before they were sacrificed either 2 or

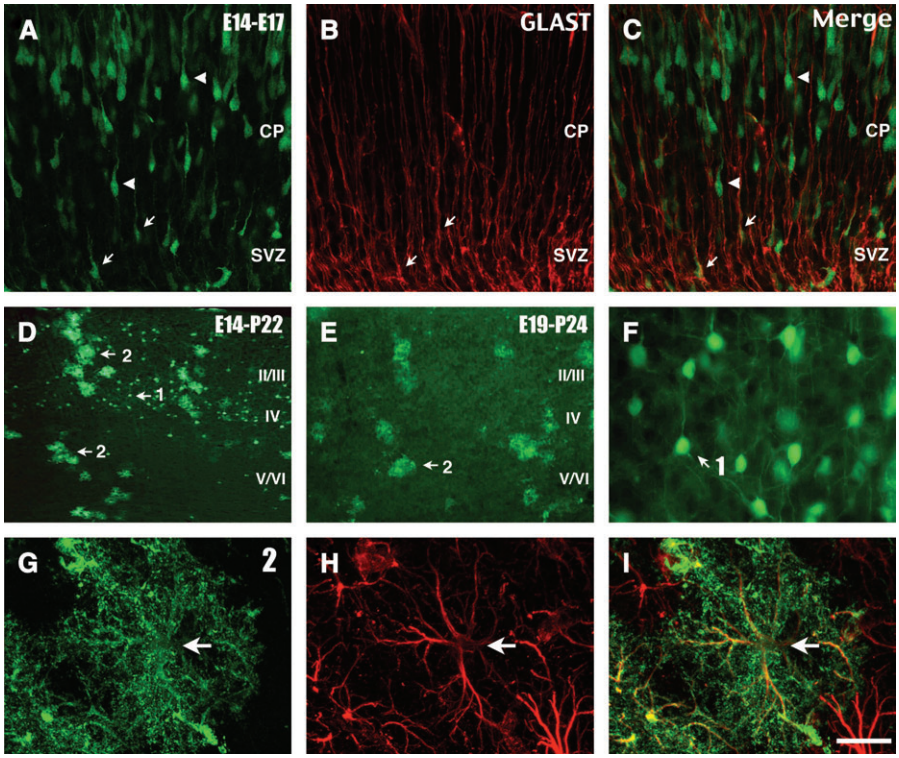

Figure 2. The nestin-CreER system detects the progeny of nestin-positive progenitors. (*A–C*) E17.5 bitransgenic embryos induced with tamoxifen at E14.5 show EGFP-expressing, GLAST-positive RGCs (arrows) as well as GLAST-negative neurons (e.g., arrowheads) migrating along RGC fibers. (*D–F*) E14.5-tamoxifen induction labels neurons (1, see *F* for higher magnification) and extensively branched astroglia (2, see *G–I* for higher magnification) in the cerebral cortex of postnatal (P22) bitransgenic mice. E18.5-tamoxifen induction labels astroglia (Kempermann 2005) but not neurons in the postnatal cerebral cortex. (*G–I*) EGFP-positive astroglia express GFAP in their proximal branches and display morphology similar to that of transformed RGC. Scale bar: 40 μm in (*A–C*), 600 μm in (*D, E*); 20 μm in (*F–I*).

7 days after injury (Fig. 4*A*). Because previous studies suggested that combined cerebral ischemia–hypoxia is a stronger stimulus of aberrant DNA synthesis than focal ischemia alone (Katchanov et al. 2001; Kuan et al. 2004), we challenged the mice with either MCAO (Fig. 4) or unilateral carotid occlusion followed by hypoxia (ischemia–hypoxia, Fig. 5).

In control experiments, no EGFP-expressing cells were found in the MCAO-challenged bitransgenic mice that did not receive tamoxifen induction (Fig. 4*B*; $n = 5$), indicating that MCAO does not cause leaky EGFP expression in the nestin-CreER system. In tamoxifen-dosed and MCAO-challenged bitransgenic mice, the vast majority of EGFP-expressing cells were located in the SVZ after 2- or 7-day survival (Fig. 4*C*; $n = 5$). On the contralateral side of the brain, the signals of BrdU labeling were restricted in the SVZ and RMS (Fig. 4*D*). In contrast, on the lesion side, there were many BrdU-incorporated cells in the striatum but not in the hippocampus (Fig. 4*E,F*). Surprisingly, only very few BrdU-labeled cells in the damaged striatum also expressed EGFP (Fig. 4*G–I*). Moreover, we did not find EGFP-positive cells expressing the migratory neuroblast marker DCX (Fig. 4*J,K*), whereas we can readily detect migratory neurons expressing DCX in the RMS (Fig. 4*L*). Based on the observed distribution pattern of EGFP-positive cells, we concluded that there was very little contribution of cell replacement by the SVZ progenitors following focal cerebral ischemia.

Aberrant DNA Synthesis after Cerebral Ischemia–Hypoxia

We previously reported that severe cerebral ischemia–hypoxia produces many TUNEL and BrdU double-labeled cells in the pyramidal layer of the hippocampus of adult rodents, suggesting that apoptotic neurons undergo aberrant DNA synthesis (Kuan et al. 2004). We have since modified the ischemia–hypoxia model allowing titration of the severity of ischemic–hypoxic insult (Adhami et al. 2006). This modified model of cerebral ischemia–hypoxia allows us to test whether aberrant DNA synthesis always lead to cell death.

We found that, following a mild ischemic–hypoxic insult when the brain damage is mostly restricted to the striatum, there was still robust BrdU labeling in the hippocampus, and to a lesser degree in the striatum and cortex, in over two-thirds of the tamoxifen-dosed bitransgenic mice at 7 days after stroke (Fig. 5*A*, $n > 10$). In these animals, the dentate granule neurons and the hippocampal neurons showed a high level of BrdU immunoreactivity (Fig. 5*B*). The BrdU immunoreactivity was specific because, in control staining, there was no immuno signal in adjacent sections when the primary anti-BrdU antibody was not added (Fig. 5*C*). These BrdU-positive hippocampal neurons showed strong signals of NeuN labeling (Fig. 5*D,E*), but importantly, they were not labeled by the TUNEL staining (Fig. 5*G*). There were some EGFP-expressing cells in the hippocampus, but they were distributed outside the pyramidal cell layer and close to the posterior periventricle (arrows in Fig. 5*F,H*). Together, these results suggest that the intense BrdU incorporation in the hippocampus after cerebral ischemia–hypoxia is due to aberrant DNA synthesis, which can occur in non-apoptotic neurons.

A recent study suggested that cyclin-dependent kinase (CDK) 5 controls the cell cycle arrest of postmitotic neurons (Cicero and Herrup 2005). Consistent with this notion, we have found

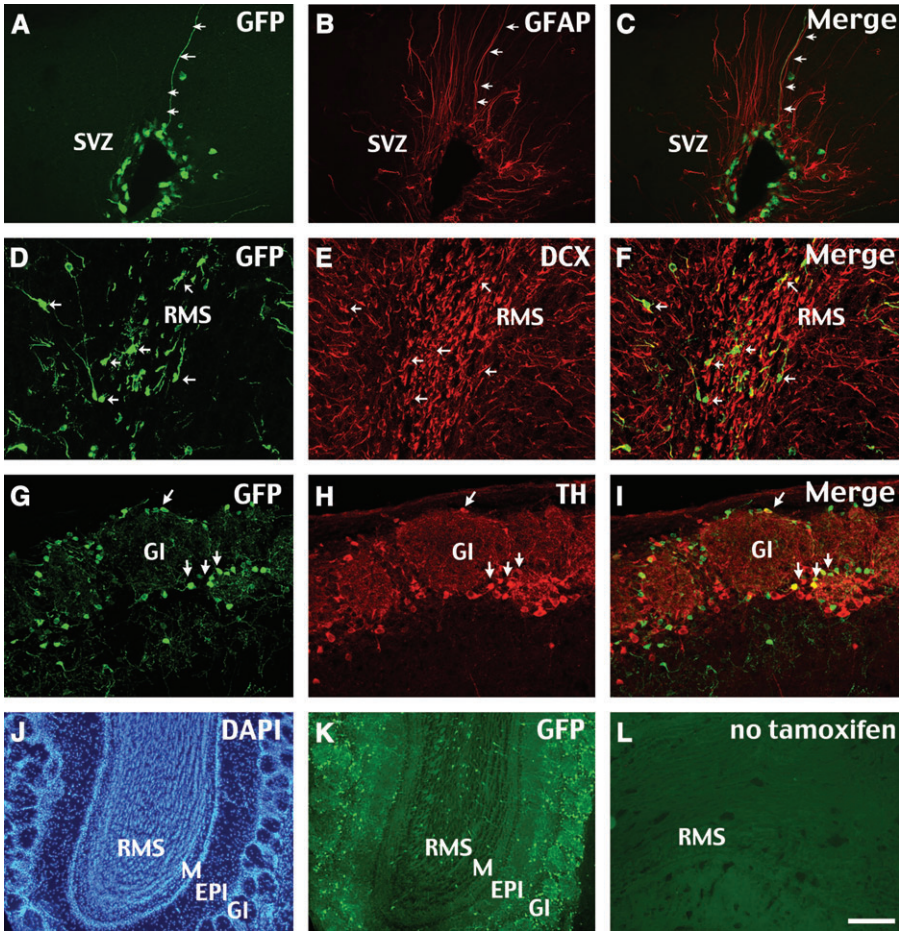

Figure 3. The nestin-CreER system labels adult neurogenesis from SVZ to olfactory bulbs. (*A–C*) Bitransgenic animals dosed with tamoxifen as adults present EGFP-labeled, GFAP-positive progenitors in the SVZ. (*D–F*) EGFP-positive cells in the RMS express DCX, a marker of migratory neurons. (*G–I*) EGFP-positive cells differentiate into periglomerular interneurons, some of which express tyrosine hydroxylase. (*J, M*) In these animals, EGFP-positive cells can be found from the SVZ to the RMS and appear to migrate through the mitral cell layer (M) and the external plexiform layer (EPL) onto the glomeruli (GL) in the olfactory bulb. (*L*) No EGFP-expressing cells were found in bitransgenic animals not receiving tamoxifen. Scale bar: 40 μm in (*A–I*); 400 μm in (*J–L*).

the protein level of CDK5 selectively reduced in the striatum and hippocampus on the lesion side, whereas the amounts of CDK2 and cyclin D1 were not obviously changed (Fig. 5*I*). Together, these results suggest that cerebral ischemia–hypoxia may disturb the cell cycle arrest state of postmitotic neurons leading to aberrant DNA synthesis.

Discussion

Nestin-CreER Mice as a Tool for Detecting Neurogenesis

There is a growing trend of developing new methods for detecting neurogenesis to complement BrdU immunocytochemistry (van Praag et al. 2002; Ahn and Joyner 2005; Spalding et al. 2005; Yu et al. 2005; Imayoshi et al. 2006). Here we report the generation of nestin-CreER mice, which detects nestin-positive progenitors and their descendant cells after tamoxifen induction. Based on the literature and our results, this seems a reasonable approximation for detecting neurogenesis. Despite some uncertainty regarding the sensitivity and specificity of nestin expression in neural progenitors, for practical purposes, the promoter and enhancer sequences of the nestin gene is a useful tool for directing transgene expression in neuroepithelial precursors that can give rise to both neurons and glia (Lendahl et al. 1990; Zimmerman et al. 1994, Kempermann 2005). The nestin promoter or enhancer sequence has been used to drive expression of the EGFP-reporter gene, allowing both the visualization of precursor cells in vivo and isolation of progenitors from adult brains (Yamaguchi et al. 2000; Kawaguchi et al. 2001; Sawamoto et al. 2001; Mignone et al. 2004). Hence, we have used the previously characterized E/nestin-hsp68 promoter (Kawaguchi et al. 2001) to generate nestin-CreER mice and examined its applications.

Our results suggest that the nestin-CreER system has several merits for neurogenesis-related research. First, when crossed to an EGFP-reporter line, this system reveals cell morphology via the cytoplasmic expression of EGFP, thus allowing for real-time imaging of progenitor proliferation and assisting in cell-type identification of their progeny. Second, the nestin–CreER system has the flexibility of temporal control of lineage tracing, which can be used to label some specific populations of cells. For example, we have shown that late-embryonic injection of tamoxifen selectively labels the astrocytically transformed RGC in the postnatal brain. This opens the possibility of prospective labeling of RGC and examining their postnatal developmental fate under experimental conditions. Third, the nestin-CreER system can be used to introduce Cre/loxP-based gene mutation in neural progenitors and to track the consequences in their descendant cells via a second Cre-dependent EGFP-reporter

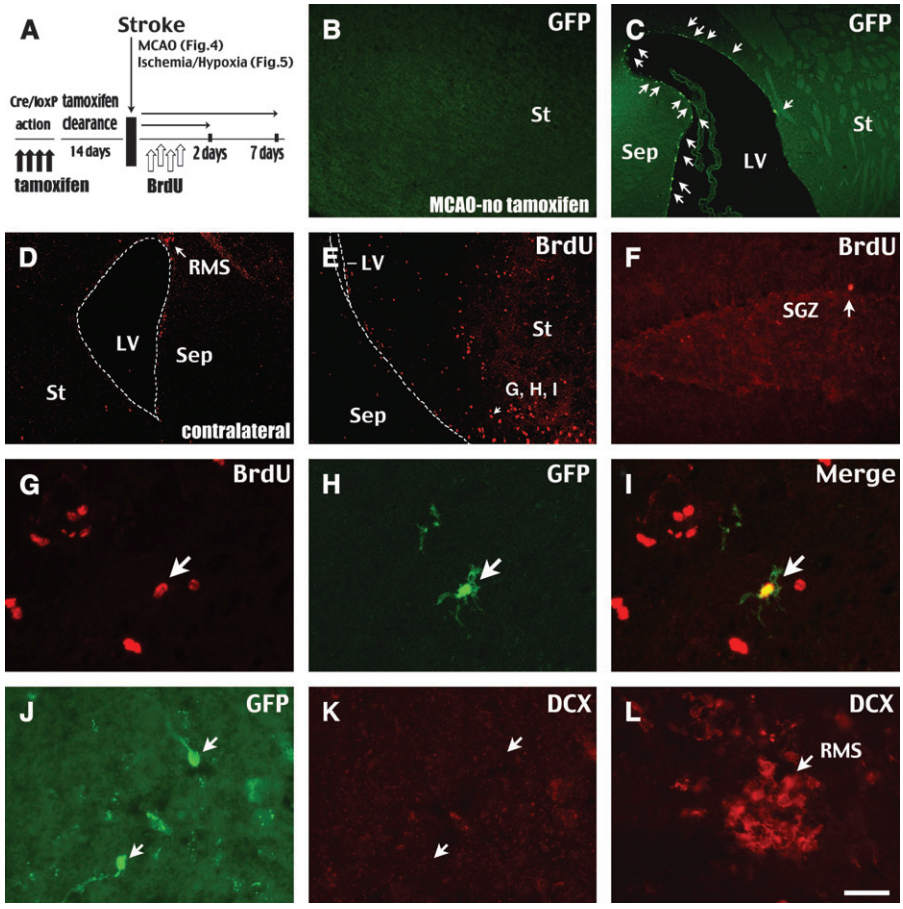

Figure 4. Cell proliferation by nestin-positive progenitors after focal cerebral ischemia. (*A*) Schematic diagram of the experimental procedure in studying poststroke neurogenesis. (*B*) No leaky EGFP-expressing cells were found in the brains of the bitransgenic mice that were challenged by the MCAO model of stroke that did not receive tamoxifen induction. (*C*) In tamoxifen-dosed and MCAO-challenged bitransgenic mice, EGFP-expressing cells were located mainly in the SVZ (arrows) but not in the surrounding striatum (St) and the septal area (Sep). (*D*) Immunocytochemistry showed normal BrdU labeling near the lateral ventricle (LV) of the contralateral hemisphere after MCAO. (*E, F*) On the lesion side, increased BrdU labeling extended into the damaged striatum (*E*) but not the hippocampus (*F*). Arrow in E indicates the location of the GFP/BrdU double-labeled cell that is illustrated in (*G–I*). (*G–I*) A small percentage of BrdU-positive cells in the stroke-damaged striatum expressed EGFP. (*J, K*) EGFP-positive cells in the stroke-damaged striatum did not express the migratory neuronal marker DCX. (*L*) As positive controls, migratory neurons in the RMS are stained by anti-DCX labeling. Scale bar: 200 μm in (*B, C*); 400 μm in (*D, E*); 40 μm in *F*; 30 μm in (*G–L*).

gene. This could be a particular useful application for identifying gene mutations in neural stem cells that cause brain tumors (Fomchenko and Holland 2005).

However, the present study also revealed several limitations of the nestin-CreER system. The most notable deficiency is that it does not label the adult dentate gyrus SGZ progenitors (false negative). This defect is consistent with E-nestin-GFP mice where no GFP was reported in the dentate gyrus of adult brains (Kawaguchi et al. 2001). We suggest that additional promoter sequences of the nestin gene may be needed to direct transgene expression in the SGZ population of adult neural progenitors (e.g., see Imayoshi et al. 2006). Also, we detected cells in brain regions that were not previously known to contribute to adult neurogenesis, and presumably, represent false-positive labeling. This may also be owing to the lack of inhibitory elements in the E-nestin construct. Alternatively, these false-positive cells may indicate a low grade or overlooked expression of nestin by nonprecursor cells in the adult brain. This should be taken into consideration when interpreting cells labeled by the nestin-CreER system: although the labeled cells descend from E-nestin–positive precursors, it remains an approximation of neurogenesis that has to be confirmed by additional methods.

Neurogenesis Versus Aberrant DNA Synthesis following Stroke

Previous studies suggested that focal cerebral ischemia stimulates the proliferation of SVZ precursors and redirects the migration of their descendants into the stroke-damage striatum (Arvidsson et al. 2002; Jin et al. 2003; Teramoto et al. 2003; Zhang et al. 2004). However, these studies primarily used BrdU incorporation combined with cell markers to detect new neurons, which could potentially include old neurons that have resumed DNA synthesis after stroke. In the present study, we have taken advantage of the ability of the nestin-CreER system to label SVZ-derived new neurons in examining this issue. Our experimental protocol includes a 2-week interval between tamoxifen induction and stroke challenge, which allows for the clearance of tamoxifen from the animal body and avoids labeling stroke-induced nestin-positive cells in the brain parenchyma that are presumably nonneurogenic (Kronenberg et al. 2005).

Surprisingly, we found only very few EGFP-positive cells derived from prelabeled SVZ progenitors, in contrast to the large number of BrdU-incorporated cells in the ischemic striatum (Fig. 4). Neither did we detect any EGFP-positive cell that expresses DCX, a marker for migrating neuroblasts.

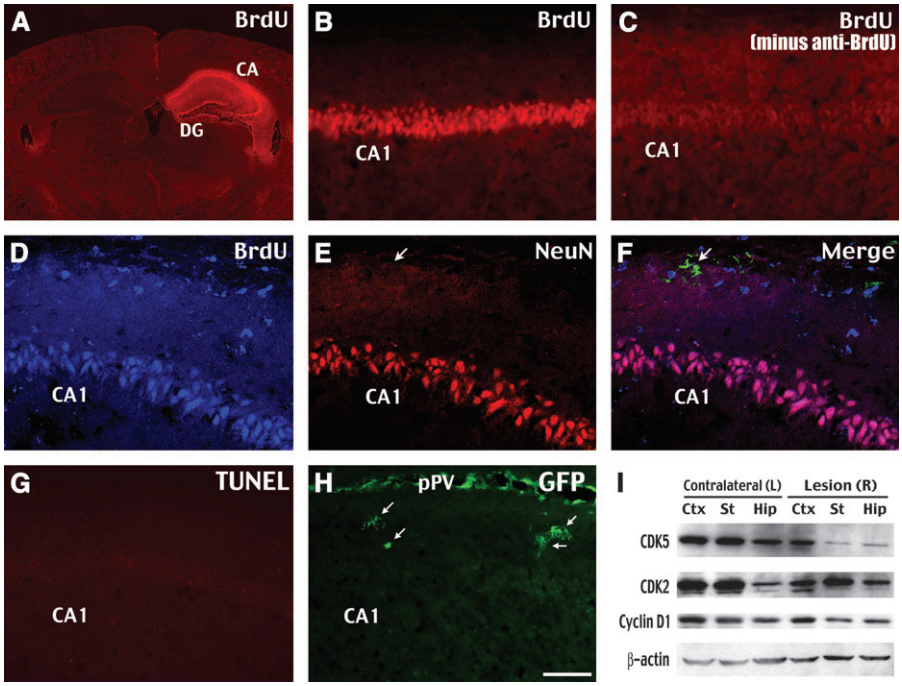

Figure 5. Aberrant BrdU incorporation following cerebral ischemia–hypoxia. (*A*) Following cerebral ischemia–hypoxia, the lesion side of the brain showed intense BrdU labeling in the hippocampus including the dentate gyrus (DG) and the Ammon's Horn (CA) sectors. (*B*) High magnification showed BrdU labeling inside the pyramidal cell layer of the CA1 sector. (*C*) Adjacent section stained with the same BrdU-immunocytochemistry protocol except without the primary (anti-BrdU) antibody showed no immunostaining signal. (*D–F*) The majority of BrdU-incorporated cells in the hippocampus expressed the neuronal marker NeuN. EGFP-positive cells (arrow) were found outside the pyramidal cell layer and did not express NeuN. (*G*) No TUNEL staining was detected in the BrdU-incorporated pyramidal cell layer, suggesting that they did not undergo cell death at least by 6 days after cerebral ischemia–hypoxia. (*H*) EGFP-expressing cells (arrows) were located near the posterior periventricle (pPV) but not in the pyramidal cell layer. (*I*) The protein level of CDK5 was reduced in the striatum (St) and the hippocampus (Hip) on the lesion side at 6 h following cerebral ischemia–hypoxia. Shown is the representative blot of 3 independent experiments. Scale bar: 60 μm in (*B, C*); 40 μm in (*D–H*).

Although we cannot exclude the possibility that neuronal replacement can occur after a longer survival period, our results are in line with previous estimations that less than 1% of BrdU-positive cells express the neuronal marker NeuN by 5 weeks after focal ischemia (Teramoto et al. 2003), and only 0.2% of deceased striatal neurons are replaced by new neurons by 6 weeks (Arvidsson et al. 2002). Thus, our results underscore the limited capacity of spontaneous neuroregeneration after stroke. Future studies are warranted using the nestin-CreER system to test whether external growth factors increase the regeneration potential of endogenous precursors.

The obvious contrast between the large number of BrdU-incorporated cells and the small number of SVZ-derived, EGFP-positive cells in stroke-challenged nestin-CreER mice raises a critical question concerning the source of these BrdU-labeled cells. Some of them may be macrophages or activated microglia. Another plausible cause of BrdU incorporation is cell cycle reentry by old neurons following brain injury (Rakic 2002; Herrup et al. 2004; Kempermann 2005). Although the concept of DNA synthesis by stressed old neurons is widely accepted, it is generally believed that this is a prelude to cell death (Liu and Greene 2001). Our previous study showing a large number of BrdU and TUNEL double-labeled hippocampal neurons following a severe ischemic–hypoxic insult also gave support to the notion that aberrant cell cycle reentry leads to immediate cell death (Kuan et al. 2004). However, the recent discovery of a large number of polyploid neurons being functionally active in healthy brains (Kingsbury et al. 2005) prompted us to reexamine whether a milder insult of cerebral ischemia–hypoxia can trigger aberrant DNA synthesis without induction of cell death.

To test this hypothesis, we have modified the cerebral ischemia–hypoxia model of stroke allowing titration of the severity of the insult (Adhami et al. 2006). Using the nestin-CreER system, here we show a large number of hippocampal neurons display a BrdU-positive, but TUNEL-negative staining profile at 7 days after a mild cerebral ischemic–hypoxic insult (Fig. 5). The lack of EGFP expression by BrdU-incorporated hippocampal neurons suggests that they are not derived from SVZ progenitors but rather due to aberrant DNA synthesis by old neurons. Thus, one cannot assume that aberrant DNA synthesis by damaged neurons will always quickly lead to cell death and therefore not confound the interpretation of neurogenesis by BrdU incorporation.

There is no simple solution to the conundrum of distinguishing de novo neurogenesis from aberrant DNA synthesis following experimental models of brain injury. However, better understanding of the mechanisms that maintain the quiescent (G0) state of postmitotic neurons and identifying the factors, such as ischemia–hypoxia, that could disrupt this cell cycle regulation may provide insights into a future solution.

Supplementary Material

Supplementary material can be found at: http://www.cercor.oxfordjournals.org/.

Notes

We thank Drs A. McMahon and S. Goldman for providing plasmids, Ms S. Falcone and the Children's Hospital Medical Center transgenic core for pronuclei injection, and Ms A. Schloemer for preparation of the manuscript. KAB is recipient of a National Institutes of Health (NIH)

National Research Service Award fellowship. This work was supported by NIH grants to C-YK and PR. *Conflict of Interest*: None declared.

Address correspondence to Dr Chia-Yi Kuan, MD, PhD, Division of Developmental Biology, Room 3464, Cincinnati Children's Hospital Research Foundation, 3333 Burnet Avenue, Cincinnati, OH 45229, USA. Email: alex.kuan@cchmc.org.

References

Adhami F, Liao G, Morozov YM, Schloemer A, Schmithorst VJ, Lorenz JN, Dunn RS, Vorhees CV, Wills-Karp M, Degen JL, et al. 2006. Am J Pathol. 169:566–583.

Ahn S, Joyner AL. 2005. In vivo analysis of quiescent adult neural stem cells responding to Sonic hedgehog. Nature. 437:894–897.

Arvidsson A, Collin T, Kirik D, Kokaia Z, Lindvall O. 2002. Neuronal replacement from endogenous precursors in the adult brain after stroke. Nat Med. 8:963–970.

Carlen M, Meletis K, Barnabe-Heider F, Frisen J. 2006. Genetic visualization of neurogenesis. Exp Cell Res. 312:2851–2859.

Cicero S, Herrup K. 2005. Cyclin-dependent kinase 5 is essential for neuronal cell cycle arrest and differentiation. J Neurosci. 25:9658–9668.

Doetsch F, Caille I, Lim DA, Garcia-Verdugo JM, Alvarez-Buylla A. 1999. Subventricular zone astrocytes are neural stem cells in the adult mammalian brain. Cell. 97:703–716.

Fomchenko EI, Holland EC. 2005. Stem cells and brain cancer. Exp Cell Res. 306:323–329.

Gal JS, Morozov YM, Ayoub AE, Chatterjee M, Rakic P, Haydar TF. 2006. Molecular and morphological heterogeneity of neural precursors in the mouse neocortical proliferative zones. J Neurosci. 26:1045–1056.

Hayashi S, McMahon AP. 2002. Efficient recombination in diverse tissues by a tamoxifen-inducible form of Cre: a tool for temporally regulated gene activation/inactivation in the mouse. Dev Biol. 244:305–318.

Herrup K, Neve R, Ackerman SL, Copani A. 2004. Divide and die: cell cycle events as triggers of nerve cell death. J Neurosci. 24:9232–9239.

Imai T, Jiang M, Chambon P, Metzger D. 2001. Impaired adipogenesis and lipolysis in the mouse upon selective ablation of the retinoid X receptor alpha mediated by a tamoxifen-inducible chimeric Cre recombinase (Cre-ERT2) in adipocytes. Proc Natl Acad Sci USA. 98:224–228.

Imayoshi I, Ohtsuka T, Metzger D, Chambon P, Kageyama R. 2006. Temporal regulation of Cre recombinase activity in neural stem cells. Genesis. 44:233–238.

Jin K, Sun Y, Xie L, Peel A, Mao XO, Batteur S, Greenberg DA. 2003. Directed migration of neuronal precursors into the ischemic cerebral cortex and striatum. Mol Cell Neurosci. 24:171–189.

Katchanov J, Harms C, Gertz K, Hauck L, Waeber C, Hirt L, Priller J, von Harsdorf R, Bruck W, Hortnagl H, et al. 2001. Mild cerebral ischemia induces loss of cyclin-dependent kinase inhibitors and activation of cell cycle machinery before delayed neuronal cell death. J Neurosci. 21:5045–5053.

Kawaguchi A, Miyata T, Sawamoto K, Takashita N, Murayama A, Akamatsu W, Ogawa M, Okabe M, Tano Y, Goldman SA, et al. 2001. Nestin-EGFP transgenic mice: visualization of the self-renewal and multipotency of CNS stem cells. Mol Cell Neurosci. 17:259–273.

Kempermann G. 2005. Adult neurogenesis. London: Oxford Press. 426 p.

Kingsbury MA, Friedman B, McConnell MJ, Rehen SK, Yang AH, Kaushal D, Chun J. 2005. Aneuploid neurons are functionally active and integrated into brain circuitry. Proc Natl Acad Sci USA. 102:6143–6147.

Kronenberg G, Wang LP, Synowitz M, Gertz K, Katchanov J, Glass R, Harms C, Kempermann G, Kettenmann H, Endres M. 2005. Nestin-expressing cells divide and adopt a complex electrophysiologic phenotype after transient brain ischemia. J Cereb Blood Flow Metab. 25:1613–1624.

Kuan CY, Schloemer AJ, Lu A, Burns KA, Weng WL, Williams MT, Strauss KI, Vorhees CV, Flavell RA, Davis RJ, et al. 2004. Hypoxia-ischemia induces DNA synthesis without cell proliferation in dying neurons in adult rodent brain. J Neurosci. 24:10763–10772.

Lendahl U, Zimmerman LB, McKay RD. 1990. CNS stem cells express a new class of intermediate filament protein. Cell. 60:585–595.

Liu DX, Greene LA. 2001. Neuronal apoptosis at the G1/S cell cycle checkpoint. Cell Tissue Res. 305:217–228.

Longa EZ, Winstein PR, Carlson S, Cummins R. 1989. Reversible middle cerebral artery occlusion without craniectomy in rats. Stroke. 20:84–91.

Mignone JL, Kukekov V, Chiang AS, Steindler D, Enikolopov G. 2004. Neural stem and progenitor cells in nestin-GFP transgenic mice. J Comp Neurol. 469:311–324.

Nakamura T, Colbert MC, Robbins J. 2006. Neural crest cells retain multipotential characteristics in the developing valves and label the cardiac conduction system. Circ Res. 98:1547–1554.

Noctor SC, Flint AC, Weissman TA, Dammerman RS, Kriegstein AR. 2001. Neurons derived from radial glial cells establish radial units in neocortex. Nature. 409:714–720.

Nowakowski RS, Hayes NL. 2000. New neurons: extraordinary evidence or extraordinary conclusion? Science. 288:771.

Rakic P. 2002. Adult neurogenesis in mammals: an identity crisis. J Neurosci. 22:614–618.

Rehen SK, McConnell MJ, Kaushal D, Kingsbury MA, Yang AH, Chun J. 2001. Chromosomal variation in neurons of the developing and adult mammalian nervous system. Proc Natl Acad Sci USA. 98:13361–13366.

Sawamoto K, Yamamoto A, Kawaguchi A, Yamaguchi M, Mori K, Goldman SA, Okano H. 2001. Direct isolation of committed neuronal progenitor cells from transgenic mice coexpressing spectrally distinct fluorescent proteins regulated by stage-specific neural promoters. J Neurosci Res. 65:220–227.

Schmechel DE, Rakic P. 1979. A golgi study of radial glial cells in developing monkey telencephalon: morphogenesis and transformation into astrocytes. Anat Embryol. 156:115–152.

Spalding KL, Bhardwaj RD, Buchholz BA, Druid H, Frisen J. 2005. Retrospective birth dating of cells in humans. Cell. 122:133–143.

Teramoto T, Qiu J, Plumier JC, Moskowitz MA. 2003. EGF amplifies the replacement of parvalbumin-expressing striatal interneurons after ischemia. J Clin Invest. 111:1125–1132.

van Praag H, Schinder AF, Christie BR, Toni N, Palmer TD, Gage FH. 2002. Functional neurogenesis in the adult hippocampus. Nature. 415:1030–1034.

Voigt T. 1989. Development of glial cells in the cerebral wall of ferrets: direct tracing of their transformation from radial glia into astrocytes. J Comp Neurol. 289:74–88.

Yamaguchi M, Saito H, Suzuki M, Mori K. 2000. Visualization of neurogenesis in the central nervous system using nestin promoter-GFP transgenic mice. Neuroreport. 11:1991–1996.

Yu TS, Dandekar M, Monteggia LM, Parada LF, Kernie SG. 2005. Temporally regulated expression of Cre recombinase in neural stem cells. Genesis. 41:147–153.

Zhang R, Zhang Z, Wang L, Wang Y, Gousev A, Zhang L, Ho KL, Morshead C, Chopp M. 2004. Activated neural stem cells contribute to stroke-induced neurogenesis and neuroblast migration toward the infarct boundary in adult rats. J Cereb Blood Flow Metab. 24:441–448.

Zimmerman L, Parr B, Lendahl U, Cunningham M, McKay R, Gavin B, Mann J, Vassileva G, McMahon A. 1994. Independent regulatory elements in the nestin gene direct transgene expression to neural stem cells or muscle precursors. Neuron. 12:1–24.